

# The Unexpected, Long-Lasting, UV Rebrightening of the Super-Luminous Supernova ASASSN-15lh

D. Godoy-Rivera<sup>1\*</sup>, K. Z. Stanek<sup>1,2</sup>, C. S. Kochanek<sup>1,2</sup>, Ping Chen<sup>3</sup>, Subo Dong<sup>4</sup>, J. L. Prieto<sup>5,6</sup>, B. J. Shappee<sup>7,8</sup>, S. W. Jha<sup>9</sup>, R. J. Foley<sup>10</sup>, Y.-C. Pan<sup>11</sup>, T. W.-S. Holoien<sup>1,2</sup>, Todd A. Thompson<sup>1,2</sup>, D. Grupe<sup>12</sup> and J. F. Beacom<sup>1,2,13</sup>

<sup>1</sup> Department of Astronomy, The Ohio State University, 140 West 18th Avenue, Columbus, OH 43210, USA

<sup>2</sup> Center for Cosmology and AstroParticle Physics (CCAPP), The Ohio State University, 191 W. Woodruff Ave., Columbus, OH 43210, USA

<sup>3</sup> Department of Astronomy, Peking University, Yi He Yuan Road 5, Hai Dian District, Beijing 100871, China

<sup>4</sup> Kavli Institute for Astronomy and Astrophysics, Peking University, Yi He Yuan Road 5, Hai Dan District, Beijing, China

<sup>5</sup> Núcleo de Astronomía de la Facultad de Ingeniería y Ciencias, Universidad Diego Portales, Av. Ejército 441, Santiago, Chile

<sup>6</sup> Millennium Institute of Astrophysics, Santiago, Chile

<sup>7</sup> Carnegie Observatories, 813 Santa Barbara Street, Pasadena, CA 91101, USA

<sup>8</sup> Hubble and Carnegie-Princeton Fellow

<sup>9</sup> Department of Physics and Astronomy, Rutgers, The State University of New Jersey, 136 Frelinghuysen Road, Piscataway, NJ 08854, USA

<sup>10</sup> Department of Astronomy and Astrophysics, University of California, Santa Cruz, CA 95064, USA

<sup>11</sup> Astronomy Department, University of Illinois at Urbana-Champaign, 1002 W. Green Street, Urbana, IL 61801, USA

<sup>12</sup> Department of Earth and Space Science, Morehead State University, 235 Martindale Dr., Morehead, KY 40351, USA

<sup>13</sup> Department of Physics, The Ohio State University, 191 W. Woodruff Ave, Columbus, OH 43210, USA

15 February 2017

## ABSTRACT

Given its peak luminosity and early-time spectra, ASASSN-15lh was classified as the most luminous supernova (SN) ever discovered (Dong et al. 2016). Here we report a UV rebrightening of ASASSN-15lh observed with *Swift* during our follow-up campaign. The rebrightening began at  $t \simeq 90$  days (observer frame) after the primary peak and was followed by a  $\sim 120$ -day long plateau in the bolometric luminosity, before starting to fade again at  $t \simeq 210$  days. ASASSN-15lh rebrightened in the *Swift* UV bands by  $\Delta m_{UVW2} \simeq -1.75$  mag,  $\Delta m_{UVM2} \simeq -1.25$  mag, and  $\Delta m_{UVW1} \simeq -0.8$  mag, but did not rebrighten in the optical bands. Throughout its initial decline, subsequent rebrightening, and renewed decline, the spectra did not show evidence of interactions between the ejecta and circumstellar medium (CSM) such as narrow emission lines. There are hints of weak H $\alpha$  emission at late-times, but Margutti et al. (2016) have shown that it is narrow line emission consistent with star formation in the host nucleus. By fitting a blackbody we find that during the rebrightening the effective photospheric temperature increased from  $T_{BB} \simeq 11000$  K to  $T_{BB} \simeq 18000$  K. Over the  $\sim 550$  days since its detection, ASASSN-15lh has radiated  $\sim 1.7\text{--}1.9 \times 10^{52}$  ergs. Although its physical nature remains uncertain, the evolution of ASASSN-15lh's photospheric radius, its radiated energy, and the implied event rate, are all more similar to those of H-poor superluminous supernovae (SLSNe-I) than to tidal disruption events (TDEs).

**Key words:** supernovae: general - supernovae: individual: ASASSN-15lh

## 1 INTRODUCTION

The discovery of super-luminous supernovae (SLSNe) (Quimby et al. 2011; Gal-Yam 2012) came as a surprise to the astronomical community despite many decades of

research on supernovae (SNe). One reason is that SLSNe appear predominantly in dwarf galaxies (Neill et al. 2011; Stoll et al. 2011; Lunnan et al. 2015), which were not well observed in early, local, targeted SN surveys that concentrated on large star-forming galaxies. SLSNe are now being systematically observed by wide-field surveys, starting with the Texas Supernova Search (TSS; Quimby 2006), and now

\* e-mail: godoyrivera.1@osu.edu

including the All-Sky Automated Survey for SuperNovae (ASAS-SN<sup>1</sup>; Shappee et al. 2014), the Palomar Transient Factory (PTF; Law et al. 2009; Rau et al. 2009), and the Panoramic Survey Telescope and Rapid Response System (Pan-STARRS; Kaiser et al. 2002). SLSNe, while rare, have the potential to illuminate our understanding of all terminal stellar explosions, not just the most extreme.

As the community was getting used to the extreme being normal with SLSNe, we discovered ASASSN-15lh (Dong et al. 2016), which strains theories for SLSN explosion mechanisms. At a redshift of  $z = 0.2326$ , ASASSN-15lh was discovered on 2015 June 14 by ASAS-SN, a project designed to monitor the entire visible sky on rapid cadence, looking for bright transients (Shappee et al. 2014). ASASSN-15lh reached a peak bolometric luminosity of  $(2.2 \pm 0.2) \times 10^{45}$  ergs s<sup>-1</sup> and radiated  $(1.1 \pm 0.2) \times 10^{52}$  ergs in the first four months of observations (Dong et al. 2016). Its early-time spectra are reasonably matched by the spectra of type I (H-poor) SLSNe (SLSNe-I). Its host, APMUKS(BJ) B215839.70615403.9 (Maddox et al. 1990), in contrast to the typical hosts of SLSNe, is a luminous ( $M_K \simeq -25.5$ ) galaxy with a low star-formation rate and a high total mass.

In this paper we report a significant UV rebrightening episode, initially noted by Brown (2015), lasting  $\sim 160$  days and dominated by a  $\sim 120$ -day long plateau in the bolometric luminosity. This rebrightening, although unexpected, should help to constrain models for the most luminous SN ever discovered, and provide new insights into the poorly understood physics and mechanisms that power SLSNe-I.

In §2 we present photometric and spectroscopic data taken during our follow-up campaign. In §3 we use these data to model the temporal evolution of the bolometric luminosity, effective photospheric temperature and radius of the source, as well as its spectral energy distribution (SED). In §4 we calculate the energy radiated by ASASSN-15lh, briefly comment on the still unknown power source and nature of the rebrightening, and compare its properties to the tidal disruption events (TDEs) discovered by ASAS-SN and other SLSNe. We summarize our results in §5.

## 2 PHOTOMETRY AND SPECTROSCOPY

In this section we present our follow-up photometric and spectroscopic observations of ASASSN-15lh. For consistency we describe the complete period of observation ( $\sim 550$  days) from the first detection of the transient on MJD 57150 through MJD 57704. The data for the period before MJD 57283.4 were already presented in Dong et al. (2016). Between MJD 57399.5 and MJD 57427.5 our follow-up campaign was suspended due to Sun constraints.

### 2.1 Photometric Observations

ASASSN-15lh was extensively observed by *Swift*. We use the series of X-ray telescope (XRT; Burrows et al. 2005) and UV/Optical telescope (UVOT; Roming et al. 2005) target-of-opportunity (ToO) observations taken between MJD 57197 and MJD 57704. The UVOT observations were

obtained in six filters: *V* (5468 Å), *B* (4392 Å), *U* (3465 Å), *UVW1* (2600 Å), *UVM2* (2246 Å), and *UVW2* (1928 Å) (Poole et al. 2008). To extract the source and sky counts we used  $\sim 5''.0$  and  $\sim 40''.0$  radii regions, respectively, using the software task UVOTSOURCE. The measured count rates were converted into magnitudes and fluxes using standard UVOT calibrations (Poole et al. 2008; Breeveld et al. 2010). The magnitudes obtained here, especially for the UV bands, are slightly different from the ones in Dong et al. (2016) because of updates to the UVOTSOURCE calibration database. The *Swift* photometric data are presented in Table 1.

During the observations, the XRT operated in Photon Counting mode (Hill et al. 2004). The X-ray data taken between MJD 57197 and MJD 57704 were combined and reduced using the software tasks XRTPipeline and XSELECT to produce a 0.3–10 keV image. The total exposure time is 232 ks. To extract the source and sky counts we used regions of radius 10 pixels ( $\sim 23''.6$ ) and 100 pixels ( $\sim 236''$ ), respectively. We do not detect X-ray emission from ASASSN-15lh with a  $3\sigma$  upper limit of  $\sim 1.1 \times 10^{-4}$  counts s<sup>-1</sup> using the Bayesian inference method described by Kraft, Burrows & Nousek (1991). Assuming a standard power law spectrum with  $\Gamma = 2$ , this implies a flux limit of  $< 6 \times 10^{-15}$  ergs cm<sup>-2</sup> s<sup>-1</sup>, or given the host luminosity distance of  $d \simeq 1170$  Mpc (Dong et al. 2016), a luminosity limit of  $L_X \leq 9.8 \times 10^{41}$  ergs s<sup>-1</sup> ( $\leq 2.6 \times 10^8 L_\odot$ ) (see also Brown et al. 2016c).

Only the combined X-ray image was considered since the constraints for individual epochs are weaker. In Dong et al. (2016) we used the same procedure to derive a  $3\sigma$  X-ray flux limit of  $< 1.6 \times 10^{-14}$  ergs cm<sup>-2</sup> s<sup>-1</sup> in the same energy range from a total exposure of 81 ks between MJD 57197 and MJD 57283. The updated X-ray limit presented here is more stringent than the one reported in Dong et al. (2016) due to the longer observation period. This limit is consistent with the X-ray detection of ASASSN-15lh at a flux of  $\sim 4 \times 10^{-15}$  ergs cm<sup>-2</sup> s<sup>-1</sup> reported by Margutti et al. (2016). The origin of the X-ray emission is unclear, and time variability is likely required for a useful interpretation.

In addition to the *Swift* observations, we also obtained *V*- and *B*-band photometry with the Las Cumbres Observatory Global Telescope Network (LCOGT; Brown et al. 2013) 1-m telescopes located at Siding Spring Observatory, South African Astronomical Observatory, and Cerro Tololo Inter-American Observatories. The images were reduced following standard procedures. We measured instrumental magnitudes using aperture photometry with a 6-pixel aperture radius ( $\sim 3''.0$ ) and then used AAVSO Photometric All-Sky Survey (APASS; Henden et al. 2015) reference stars in the field to obtain calibrated Johnson-Cousins magnitudes for our target. The resulting magnitudes are slightly different from the ones of Dong et al. (2016) because here we used a larger number of reference stars in the calibration. The LCOGT photometric data are presented in Table 2.

As explained in Dong et al. (2016), we also have ASAS-SN *V*-band pre-discovery images that allow us to date the detection of ASASSN-15lh to MJD 57150. These data provide the only photometric observations for the period before MJD 57189.4.

Given that the *V*- and *B*-band of *Swift* and LCOGT are not identical, we translated the LCOGT magnitudes to the *Swift* system by deriving offsets between the two datasets. The offsets were calculated using linear interpolation

<sup>1</sup> <http://www.astronomy.ohio-state.edu/~assassin/>

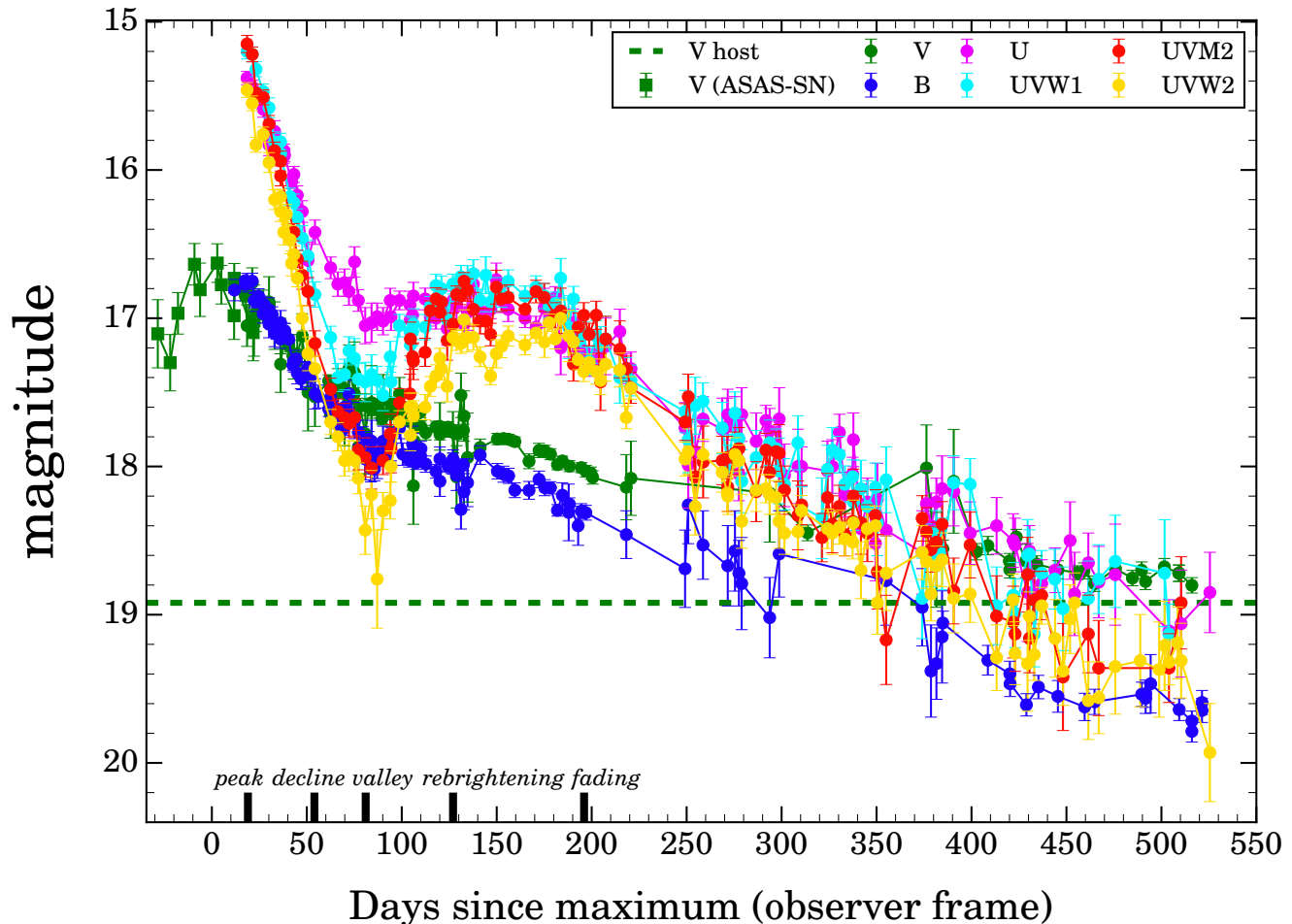


**Figure 1.** Light curves of ASASSN-15lh in the observer frame spanning from 29 days before maximum through 525 days after maximum (MJD 57150 to MJD 57704). The *Swift* and LCOGT follow-up data are shown as filled circles, and the ASAS-SN *V*-band data are shown as green squares. The synthetic host galaxy magnitude of  $V = 18.92$  (Dong et al. 2016) is shown as the green horizontal dashed line. All magnitudes are in the Vega system as measured by *Swift*, and were not corrected for extinction or the host contribution. Representative dates for the different stages of the light curve evolution (see §2.1) are shown as black vertical lines at the bottom.

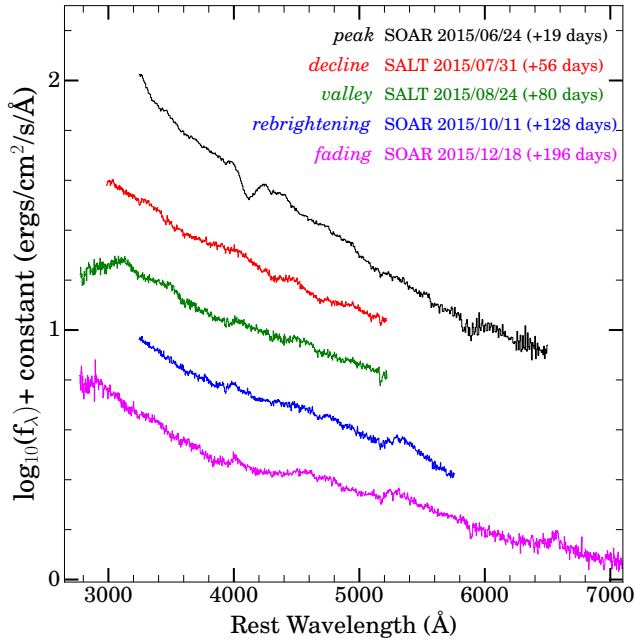
of the LCOGT measurements for the initial period where we have overlapping observations (MJD 57196.5 to MJD 57308.5). We obtained  $\Delta V = -0.052$  and  $\Delta B = +0.026$ , where  $\Delta m = m_{\text{Swift}} - m_{\text{LCOGT}}$ .

Figure 1 shows the light curves of ASASSN-15lh from its first detection at MJD 57150 through MJD 57704. The source magnitudes shown in Figure 1 are not corrected for the host contribution or Galactic extinction. All *V*- and *B*-band magnitudes are shown in the *Swift* system. The synthetic *V*-band magnitude of the host galaxy that we derived in Dong et al. (2016) by modeling its SED is also shown. Hereafter the times will be expressed relative to the maximum of the ASAS-SN *V*-band light curve (MJD 57178.5; Dong et al. 2016) in the observer frame, unless otherwise stated.

The evolution of the light curve is striking. After the maximum, ASASSN-15lh showed a continuous decline at all wavelengths. Then, near  $t \simeq 90$  days, a rebrightening began in the UV bands. Figure 1 shows that the rebrightening is largest for the bluer bands:  $\Delta m_{UVW2} \simeq -1.75$  mag (peak at  $t \simeq 133$  days),  $\Delta m_{UVM2} \simeq -1.25$  mag (peak at  $t \simeq$

133 days), and  $\Delta m_{UVW1} \simeq -0.8$  mag (peak at  $t \simeq 138$  days). While this happened in the UV, the *U*-band remained roughly constant for 97 days (a standard deviation of  $\sigma_U \simeq 0.08$  mag between  $t \simeq 84$  days and  $t \simeq 181$  days), and the *V*- and *B*-band continued to slowly decline.

We identify five distinct phases in the multi-wavelength light curve of ASASSN-15lh, and note corresponding representative dates: the *peak* ( $t \simeq 19$  days), where all the bands had their maximum brightness, except for the *V*-band (which had its maximum around  $t = 0$  in the ASAS-SN data); a following *decline* ( $t \simeq 54$  days), where all the bands declined roughly monotonically; the *valley* ( $t \simeq 81$  days), where the UV+*U* bands reached their first minimum; the unexpected *rebrightening* ( $t \simeq 127$  days) that was seen in the UV and not in the optical (although the *U*-band stopped declining); and finally a *fading* stage ( $t \simeq 196$  days), where all bands again declined monotonically. The representative dates of these stages are shown as black vertical lines at the bottom of Figure 1. In §2.2 we show spectra selected to approximately match these representative dates.



**Figure 2.** Rest frame spectroscopic evolution of ASASSN-15lh. Spectra dates were selected to represent the different stages of the light curve evolution of Figure 1 (see § 2.1). The dates of the observations in UT time, and with respect to the light curve maximum (in the observer frame), are shown together with the instrument used and the name of the phase. The colors of the spectra match the corresponding date and instrument. Offsets have been added to the spectra for clarity.

## 2.2 Spectroscopic Observations

In the first  $\sim 330$  days after the detection of ASASSN-15lh, we obtained numerous spectra. Here we show only a representative sample, illustrating the five stages defined in §2.1, and other late-time epochs. Spectra were obtained with the Robert Stobie Spectrograph (Smith et al. 2006) on the 10-m Southern African Large Telescope (SALT), the Goodman Spectrograph (Clemens, Crain & Anderson 2004) on the 4-m Southern Astrophysical Research Telescope (SOAR), the Magellan Echellette (MagE; Marshall et al. 2008) Spectrograph on the 6.5-m Baade telescope, and the Wide Field CCD (WFCCD) camera on the 2.5-m du Pont telescope.

The SALT data were taken with a  $1''.5$  wide longslit (oriented to  $PA=127.7^\circ$  east of north) and used the PG0900 grating, resulting in a spectral resolution of  $\lambda/\Delta\lambda \approx 900$ . The 2015 July 31 and 2015 August 24 observations used two tilt positions to cover the wavelength range from 3500–6400 Å (without chip gaps) with a total exposure time of 2240 s. The data were reduced with a custom pipeline that incorporates routines from PyRAF and PySALT (Crawford et al. 2010).

The SOAR observations used an  $1''.07$  wide longslit with the “M1” blue (for all epochs) and “M2” red (for the December epoch; the GG455 order-blocking filter was also used) 400-line VPH gratings. Standard CCD processing and spectral extraction were accomplished with IRAF<sup>2</sup>. The data

<sup>2</sup> IRAF: the Image Reduction and Analysis Facility is distributed by the National Optical Astronomy Observatory, which is oper-

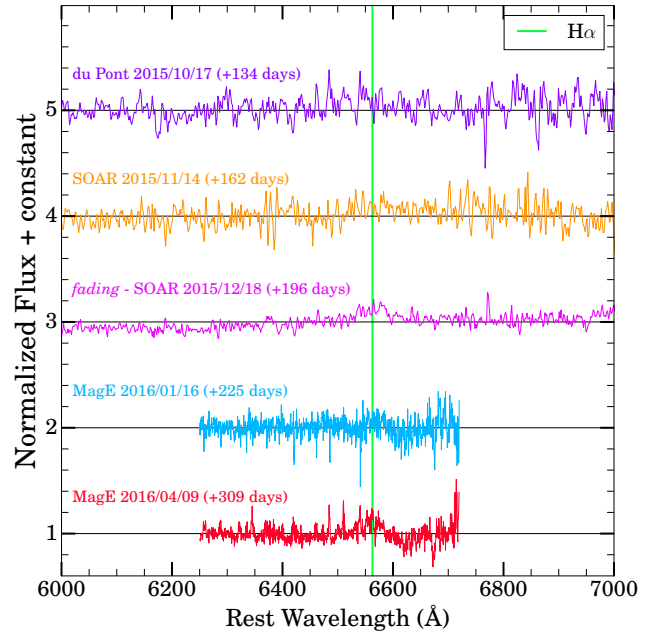


**Figure 3.** Rest frame spectroscopic evolution of ASASSN-15lh near the wavelength of  $H\alpha$ . The spectra were normalized by a 2nd-degree polynomial fit to the continuum to emphasize on the relative strength of any potential features. The spectra were selected to cover the period before and after the SOAR spectrum of the *fading* stage ( $t = 196$  days). The dates of the observations in UT time, and with respect to the light curve maximum (in the observer frame), are shown together with the instrument used. For the MagE spectra, only the orders containing the wavelength of  $H\alpha$  were used in the continuum fit. The colors of the spectra have an arbitrary flux offset and a horizontal line is drawn at the mean of each spectrum. The expected position of  $H\alpha$  (6562.8 Å) is shown as the vertical green line.

were extracted using the optimal algorithm of Horne (1986). Low-order polynomial fits to calibration-lamp spectra were used to establish the wavelength scale, and small adjustments derived from night-sky lines in the object frames were applied. We employed our own IDL routines to flux calibrate the data and remove telluric lines using the well-exposed continua of spectrophotometric standards (Wade & Horne 1988; Foley et al. 2003). Details of our spectroscopic reduction techniques are described by Silverman et al. (2012).

We obtained two medium-resolution ( $R \approx 4000$ ) MagE optical spectra of ASASSN-15lh on 2016 Jan 16 and 2016 April 9. We extracted the echellette orders using Dan Kelson’s MagE pipeline<sup>3</sup>. The 2015 October 17 du Pont spectrum was reduced using standard IRAF procedures.

Figure 2 shows the spectroscopic evolution of ASASSN-15lh. The shape of the spectra indicate that the source remained hot during the whole period of observation, in agreement with the blackbody fit ( $T_{\text{BB}} \gtrsim 11000$  K) to the photometric data presented in §3.

For the first  $\sim 45$  days the most prominent feature was

ated by the Association of Universities for Research in Astronomy, Inc. (AURA) under cooperative agreement with the National Science Foundation (NSF).

<sup>3</sup> <http://code.obs.carnegiescience.edu/mage-pipeline>

the absorption line near  $\sim 4100 \text{ \AA}$  (see §4.3.2 and also Figure 2 of Dong et al. 2016). This feature has also been seen in the SLSNe-I SN 2010gx (Pastorello et al. 2010), SN 2015bn (Nicholl et al. 2016b), and PTF12dam (Nicholl et al. 2013) among others, and it has been attributed to O II (Quimby et al. 2011; Inserra et al. 2013). The feature almost completely disappeared  $\sim 35$  days before the rebrightening began.

From the *decline* stage onward, the spectra show a mostly featureless continuum at all epochs, without the appearance of significant features, with the exception of the last spectrum. This SOAR spectrum taken at  $t = 196$  days (corresponding to the *fading* stage) shows a slight bump near the expected position of  $H\alpha$  ( $6562.8 \text{ \AA}$ ). No such feature is seen at early-times (see Figure 2 of Dong et al. 2016).

Since the absence of H and He emission features is one of the key points for the SLSN-I hypothesis, this feature requires further investigation. Figure 3 shows a selection of spectra chosen to display the late-time evolution of ASASSN-15lh near the wavelength of  $H\alpha$ . The spectra were normalized by a smooth continuum to study the relative strength of any feature. The SOAR spectrum at  $t = 196$  days is the only one with significant evidence for a bump near  $H\alpha$ . The du Pont spectrum at  $t = 134$  days, and the SOAR spectrum at  $t = 162$  days, do not show significant features at that wavelength. The MagE spectra at  $t = 225$  days and at  $t = 309$  days show hints of features near the  $H\alpha$  wavelength, but are also strongly affected by the quality of the telluric corrections and noise. We cannot definitively determine if the feature seen near the wavelength of  $H\alpha$  is an instrumental artifact, the effect of telluric lines, or a weak, transient broad  $H\alpha$  emission line.

Milisavljevic et al. (2015) also report no sign of broad  $H\alpha$  emission at  $t = 135$  days, while Leloudas et al. (2016) claim a  $H\alpha$  detection (FWHM  $\simeq 2500 \text{ km s}^{-1}$ ) at  $t = 37$  days. If real, the broad  $H\alpha$  emission would still be energetically negligible. It would be about  $\sim 20$  times weaker relative to the continuum than the  $H\alpha$  emission observed in the SLSN-I iPTF13ehe (Yan et al. 2015). More importantly, Margutti et al. (2016) clearly identify narrow  $H\alpha$  and [N II] emission in a spectrum taken at  $t = 301$  days, and convincingly argue that all the evidence for  $H\alpha$  emission from the transient is simply a blend of these emission lines produced by star formation in the nucleus of the host galaxy.

### 3 SED, LUMINOSITY AND EFFECTIVE TEMPERATURE EVOLUTION

As seen in Figure 1, our UV monitoring was continuous except for the Sun constraint break ( $221 \text{ days} < t < 249 \text{ days}$ ). In addition, the *Swift*  $V$  and  $B$ -band observations were interrupted between  $t = 135$  days and  $t = 188$  days due to their absence in the ToO requests during that period, but the gap was covered by the LCOGT photometry. After  $t = 188$  days *Swift* began to observe the source in the optical bands again, although not always including both the  $V$  and  $B$ -bands simultaneously. The LCOGT photometry was again used when needed.

We obtained fluxes in each band by correcting for Galactic extinction, assuming  $E(B - V) = 0.03 \text{ mag}$  (Schlafly & Finkbeiner 2011), and subtracting the host galaxy contribu-

tion. The fluxes were fit to blackbody models using Markov Chain Monte Carlo (MCMC) methods to derive luminosities, photospheric effective temperatures, and apparent photospheric radii. While the light curves of Figure 1 include all the photometric data, for  $t < 221$  days (beginning of Sun constraint break) the SED calculations and blackbody fits only use epochs for which the *Swift* magnitudes satisfy  $\sigma_m \leq 0.2$ , the LCOGT magnitudes satisfy  $\sigma_m \leq 0.10$ , and the four UV bands have measured magnitudes. These quality cuts were not used for the period after the Sun constraint break, when the target was fainter, given the lower signal-to-noise ratio of the observations.

As in Dong et al. (2016), for epochs earlier than  $t = 12$  days, when the photometry relied only on ASAS-SN  $V$ -band data, we used two different priors on the blackbody temperature. One extrapolates between  $t = 12.5$  days and  $t = 62.5$  days and increases linearly in logarithmic scale towards earlier times, while the other assumes a constant temperature (the one at  $t = 12.5$  days) for those epochs. After  $t = 12.5$  days we did not use any prior on the temperature because *Swift* started observing ASASSN-15lh and UV photometry became available. The numerical values of the blackbody models are presented in Tables 3, 4, and 5. Our results for the bolometric luminosity roughly agree with those presented by Brown et al. (2016c).

Figure 4 shows the observed and best-fit blackbody SED evolution, matching the five stages highlighted before. Models with the constant-temperature prior at early-times for the bolometric luminosity, effective temperature, and apparent photospheric radius are shown as the green symbols in Figures 5, 6, and 7, respectively. For comparison and discussion (see §4.3), the same quantities are also shown for the three ASAS-SN TDEs (Holoien et al. 2014, 2016a,b; Brown et al. 2016a,b) and for a sample of SLSNe-I with available late-time data.

The effects of the UV rebrightening are visible in Figure 4. From the *peak* through the *decline* and into the *valley* phases, the SED of ASASSN-15lh showed a monotonic decrease in luminosity while getting redder with a decreasing effective temperature. Later, when the *rebrightening* occurred, these trends reversed. The source increased both in luminosity ( $\sim 1.4$  times) and in effective temperature ( $\sim 1.5$  times). Later on, for the *fading* stage, the SED was less luminous than during the *rebrightening*, but it was still very blue and showed an even higher effective temperature ( $T_{\text{BB}} \simeq 18000 \text{ K}$ ). This wavelength-dependent luminosity evolution shows that the “additional” radiation (in comparison with the monotonic SED decline at early-times) seen during the *rebrightening* is indeed peaking at the UV wavelengths.

The evolution of the blackbody bolometric luminosity, effective temperature, and apparent photospheric radius of ASASSN-15lh (Figures 5, 6, and 7), all show monotonic trends from the *peak* into the *valley*, with the photosphere cooling as it expands and becomes less luminous. During this time, the luminosity drops considerably, from  $L_{\text{bol}} \simeq 6.2 \times 10^{11} L_{\odot}$  to  $\simeq 1.1 \times 10^{11} L_{\odot}$ , the effective temperature drops from  $T_{\text{BB}} \simeq 20000 \text{ K}$  to  $\simeq 11000 \text{ K}$ , and the photospheric radius increases from  $R_{\text{BB}} \simeq 3 \times 10^{15} \text{ cm}$  to  $\simeq 7 \times 10^{15} \text{ cm}$  (assuming the constant temperature prior at early-times). The initial rapid rise in the radius of the apparent photosphere of ASASSN-15lh roughly corresponds to

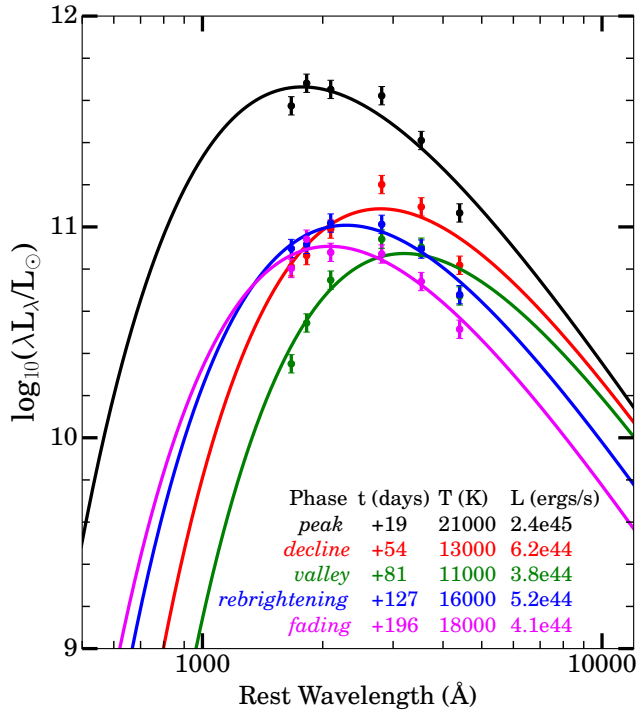


**Figure 4.** SED evolution of ASASSN-15lh. The observed SEDs are shown as filled circles while the best-fit blackbody models are shown as solid lines. These epochs correspond to the dates highlighted in Figure 1 (see §2.1), and are within 2 days of the spectroscopy epochs shown in Figure 2. The names of the phases, dates (in the observer frame), best-fit effective temperatures, and luminosities, are listed for each epoch in the corresponding color. The X-ray luminosity upper limit derived in §2.1,  $\log_{10}(L_X/L_\odot) \leq 8.4$ , and the radio luminosity upper limit reported by Kool et al. (2015),  $\log_{10}(L_{\text{Radio}}/L_\odot) \leq 4.9$ , are below the scale of the figure.

a velocity of  $\sim 4700 \text{ km s}^{-1}$ , as indicated by the purple line in Figure 7.

Then, after  $t \simeq 90$  days ( $\simeq 73$  days in the rest frame), when the UV rebrightening is seen in the multi-wavelength light curve (see Figure 1), there is a rise in the effective temperature changing from  $T_{\text{BB}} \simeq 11000 \text{ K}$  to  $\simeq 18000 \text{ K}$  at  $t \simeq 129$  days ( $\simeq 105$  days in the rest frame), and it maintains this high effective temperature even after entering the *fading* stage. After the *valley*, the luminosity shows a plateau at  $L_{\text{bol}} \simeq 1.3 \times 10^{11} L_\odot$  for roughly 120 days ( $\sim 97$  days in the rest frame). The largest increase in luminosity over this period is only of a factor of  $\approx 1.4$ . The large change in effective temperature at a nearly fixed luminosity then implies a significant drop in the apparent photospheric radius, from  $R_{\text{BB}} \simeq 6.5 \times 10^{15} \text{ cm}$  to  $R_{\text{BB}} \simeq 2.3 \times 10^{15} \text{ cm}$ . We interpret this decrease in the photospheric radius as seeing deeper into the ejecta, as the outer layers become optically thin.

After the *fading* stage, the bolometric luminosity decreases monotonically, the effective photospheric temperature oscillates with a constant overall trend, and the photospheric radius shows a decreasing trend. In the latest epochs, the luminosity has dropped to  $L_{\text{bol}} \simeq 1.6 \times 10^{10} L_\odot$ , while the photospheric radius has decreased to  $R_{\text{BB}} \simeq 1.3 \times 10^{15} \text{ cm}$ . At late-times the uncertainties in the blackbody pa-

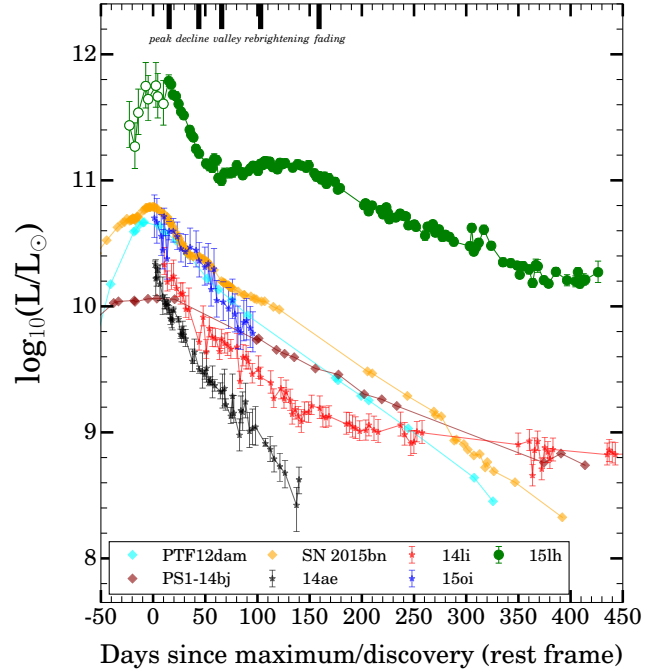


**Figure 5.** Bolometric luminosity evolution of ASASSN-15lh for blackbody fits using the constant-temperature prior (see §3) at early-times (open green circles), and no prior afterwards (filled green circles). Representative dates for the different stages of the light curve evolution of ASASSN-15lh (see Figure 1), translated to the rest frame, are shown as black vertical lines at the top. For comparison, the evolution of the same quantity is shown for the three ASAS-SN TDEs (stars, see Holoien et al. 2016a), and for a sample of SLSNe-I with late-time observations (diamonds). For all the transients, the data are shown in the rest frame with respect to either the maximum of the light curve or the discovery date.

rameters are greater because of the poorer photometry, as ASASSN-15lh gets fainter.

One possibility for explaining the behavior during the rebrightening phase is additional energy injection that both increased the effective temperature, and stabilized the bolometric luminosity. Alternatively, there could be two components to the luminosity: an optical component that continues to cool and fade with time, and a UV component that peaks at  $t \simeq 150$  days ( $\simeq 122$  days in the rest frame). This second scenario would explain the change in effective temperature without needing additional late-time energy injection, but would likely require a change in opacity to allow more UV photons to escape at late-times (but see also Metzger et al. 2014).

## 4 DISCUSSION

### 4.1 Energetics

Blackbody models, while not perfect, are commonly used for SN SED fits (for recent examples see Arcavi et al. 2016 and Nicholl et al. 2016b). Even though ASASSN-15lh SEDs show deviations from our best-fit blackbody models (see Figure 4), the approximation of its emission coming from a thermal photosphere allows us to model the bolometric luminosity



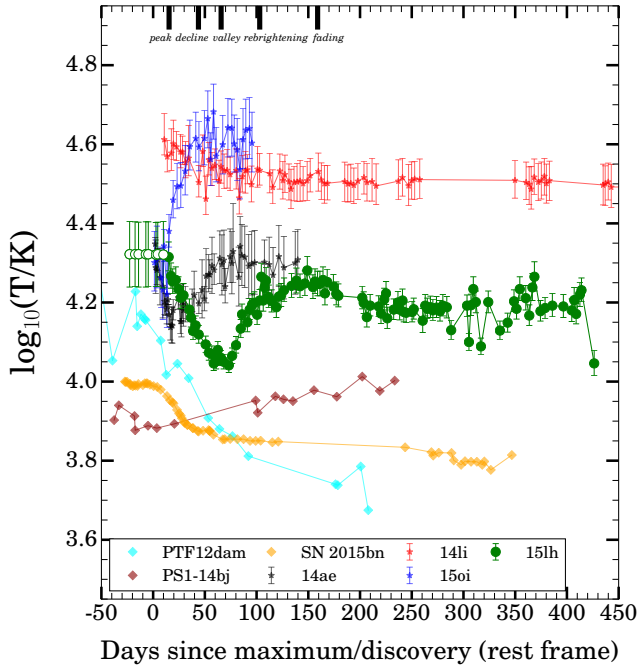


**Figure 6.** Evolution of the effective photospheric temperatures of ASASSN-15lh, the three ASAS-SN TDEs, and a sample of SLSNe-I with late-time observations. The labeling and time-axis are the same as in Figure 5.

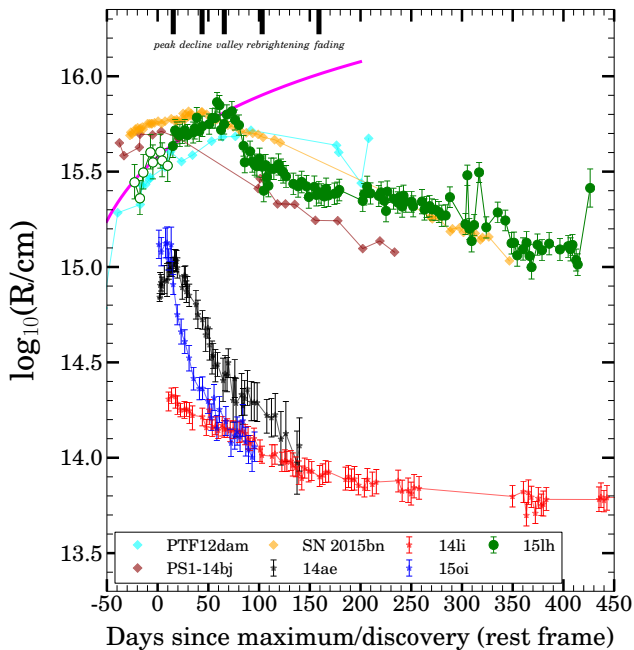


**Figure 7.** Evolution of the apparent photospheric radii of ASASSN-15lh, the three ASAS-SN TDEs, and a sample of SLSNe-I with late-time observations. The purple line shows the photospheric radius evolution expected for a constant expansion at  $\sim 4700 \text{ km s}^{-1}$  for ASASSN-15lh. The labeling and time-axis are otherwise the same as in Figures 5 and 6.

and energy of the event, in addition to obtaining estimates for the effective temperature and photospheric radius. The X-ray non-detections derived in §2.1 (or the weak detection of Margutti et al. 2016) support a roughly thermal drop off in the SED at higher energies.

Trapezoidal integration of the bolometric luminosity was used to calculate the energy emitted by ASASSN-15lh from discovery through  $t = 525$  days after maximum. We estimate the total radiated energy (in the rest frame) to be  $E \simeq 1.7 \times 10^{52}$  ergs for the constant-temperature prior, and  $E \simeq 1.9 \times 10^{52}$  ergs for the rising-temperature prior. The choice of the prior dominates the uncertainties in these estimates.

To quantify the impact of the UV rebrightening in terms of energy, we separated the integral of the bolometric luminosity from discovery ( $t \simeq -29$  days) to the *valley* stage ( $t \simeq 81$  days), and from the *valley* to the latest epoch ( $t \simeq 525$  days). ASASSN-15lh radiated  $\sim 9.6 \times 10^{51}$  ergs (56% of the total energy) before the rebrightening started, and  $\sim 7.4 \times 10^{51}$  ergs (44%) after.

## 4.2 ASASSN-15lh and its UV rebrightening in the context of SLSNe powering mechanisms

The physics behind SLSNe-I are poorly understood. Three commonly invoked mechanisms are: the radioactive decay of  $^{56}\text{Ni}$  (Gal-Yam et al. 2009; Young et al. 2010), interaction between the SN ejecta and a dense circumstellar medium (CSM) (Chevalier & Irwin 2011; Ginzburg & Balberg 2012; Chatzopoulos et al. 2013; Sorokina et al. 2016), and the spin-down of a magnetar (a highly magnetized and rapidly rotating neutron star) (Kasen & Bildsten 2010; Woosley 2010; Inerra et al. 2013).

Given the extreme  $\sim 2.2 \times 10^{45} \text{ ergs s}^{-1}$  peak bolometric luminosity, the radioactive decay of  $^{56}\text{Ni}$  is strongly disfavoured as one of the powering mechanisms for ASASSN-15lh. Recently, Kozyreva et al. (2016) estimated that a nickel mass of  $1500 M_{\odot}$  would be required to explain this peak luminosity. However, the bolometric luminosity evolution obtained for this explosion differs significantly from the observed evolution (see their Figure 3). Consequently, this mechanism can be ruled out as a plausible driver of the explosion.

For SLSNe-II (H-rich), which appear to be the high-luminosity counterparts of SNe IIn, CSM interaction seems to be the powering mechanism (Gal-Yam 2012, but see also Inerra et al. 2016). For this same mechanism to power SLSNe-I, however, the CSM would probably need to be H-poor, since no H emission lines are seen in the spectra of these events. This H-poor CSM interaction mechanism was favoured by Chatzopoulos et al. (2016) in order to explain the bolometric luminosity evolution of ASASSN-15lh, although large ejecta and CSM masses ( $\sim 36 M_{\odot}$  and  $\sim 19.5 M_{\odot}$ , respectively) would be needed. While providing a good fit to the overall luminosity evolution, detailed calculations of the expected multi-wavelength light curve are needed to see if the observed UV rebrightening can be explained in this context. More theoretical work is also needed to understand whether the absence of narrow emission lines in the spectra of ASASSN-15lh disfavours this scenario.

The magnetar model suggested by Dong et al. (2016) to explain the peak bolometric luminosity required a magnetar

with a period  $P \simeq 1$  ms and a magnetic field  $B \simeq 10^{13}$ – $10^{14}$  G, assuming efficient thermalization in the envelope, based on the models of Kasen & Bildsten (2010). These parameters could explain a radiated energy of up to  $\sim 10^{52}$  ergs, but seemed extreme for a magnetar because they pushed the model close to the point where gravitational waves losses limit the available energy (Dong et al. 2016). Nevertheless, recent studies have claimed that the total radiated energy that can be extracted from the spinning down of such magnetar might be even higher. Both Metzger et al. (2015) and Sukhbold & Woosley (2016) argue that the upper energy limits of the magnetar model are still higher and are not exceeded by ASASSN-15lh.

To reproduce the early-stages of the light curve of ASASSN-15lh with the magnetar model, Metzger et al. (2015) used an ejecta mass of  $M_{\text{ej}} = 3M_{\odot}$ . Given the ejecta mass, it is possible to make an order-of-magnitude estimate of the scale at which the ejecta should become optically thin, because the optical depth through the medium is

$$\tau \sim \kappa \Sigma \sim \kappa \frac{M_{\text{ej}}}{4\pi R^2}. \quad (1)$$

Setting  $\tau = 1$ , and using an opacity of  $0.2 \text{ cm}^2 \text{ g}^{-1}$  (Metzger et al. 2015), we can solve for  $R$  to find

$$R_{\tau=1} \sim 9.8 \times 10^{15} \text{ cm} \left( \frac{M_{\text{ej}}}{3M_{\odot}} \right)^{1/2} \left( \frac{\kappa}{0.2 \text{ cm}^2 \text{ g}^{-1}} \right)^{1/2}. \quad (2)$$

This estimate is in rough agreement with our derived blackbody radius at the time the ejecta begins to recede,  $R_{\text{bb}} \simeq 7 \times 10^{15}$  cm at  $\sim 70$  days. Even for higher ejecta masses ( $M_{\text{ej}} \simeq 11.2M_{\odot}$ , Sukhbold & Woosley 2016), or slightly different opacity values, the radius estimates are still of the same order.

The standard magnetar model predicts a power-law luminosity decay  $L_{\text{bol}} \propto t^{-2}$  (Inserra et al. 2013). This monotonic decay is obviously absent for ASASSN-15lh, given that the observed UV rebrightening is associated with a plateau phase in the bolometric luminosity. A scenario where multiple processes are involved in powering SLSNe is certainly conceivable, and observational evidence for this has been found previously. An example is iPTF13ehe (Yan et al. 2015; Wang et al. 2016), a SLSN-I that showed a late ( $\sim 250$  days in the rest frame, Yan et al. 2015)  $r$ -band rebrightening, together with the appearance of broad  $\text{H}\alpha$  emission in the spectrum. Yan et al. (2015) argued that the  $\text{H}\alpha$  feature is caused by interaction between the SN ejecta and a H-rich CSM. Moreover, Wang et al. (2016) argued that all three of the possible SLSN mechanisms we discussed above could be involved in explaining the observed spectra and light curve evolution of iPTF13ehe. A magnetar and the decay of  $^{56}\text{Ni}$  could be simultaneously powering the early-time light curve, while interactions between the SN ejecta and the CSM would be the power source at late-times.

Similarly, multiple power sources could also be powering ASASSN-15lh, as suggested by Chatzopoulos et al. (2016). ASASSN-15lh, however, differs from iPTF13ehe. The rebrightenings were seen at different rest-frame wavelengths ( $\lambda_{\text{rest}} \simeq 1600 \text{ \AA}$  for ASASSN-15lh and  $\lambda_{\text{rest}} \simeq 4600 \text{ \AA}$  for iPTF13ehe), and ASASSN-15lh shows no new prominent spectral features. It basically has a blue and mostly featureless spectrum at all times, with the hint of  $\text{H}\alpha$  being associated with star formation in the host (Margutti et al.

2016). The  $r$ -band rebrightening seen in iPTF13ehe is quite different because it was accompanied by the appearance of strong  $\text{H}\alpha$  emission.

### 4.3 Comparison of ASASSN-15lh with TDEs and SLSNe-I

#### 4.3.1 Blackbody Parameters

In Dong et al. (2016), the early-time observations of ASASSN-15lh lead us to classify the transient as a SLSN-I, given the resemblance of its spectra with such transients. Nevertheless, given that the position of ASASSN-15lh is consistent with the center of its host galaxy (angular separation of  $\sim 0''.2$ , implying a projected physical separation of  $\sim 750$  pc, Dong et al. 2016), a potential alternative interpretation for its nature is a TDE.

We compiled a list of both SLSNe-I and optically bright TDEs, preferably with late-time photometric observations, and Figures 5, 6, and 7 compare their rest-frame evolution in luminosity, temperature, and photospheric radius to ASASSN-15lh. For the TDEs, we compare with the well studied systems ASASSN-14ae (Holoien et al. 2014; Brown et al. 2016a), ASASSN-14li (Holoien et al. 2016b; Brown et al. 2016b), and ASASSN-15oi (Holoien et al. 2016a). For the SLSNe-I, we compare with PTF12-dam (Nicholl et al. 2013; Chen et al. 2015), PS1-14bj (Lunnan et al. 2016), and SN 2015bn (Nicholl et al. 2016b,a).

PS1-14bj (at  $z = 0.5215$ ), PTF12dam (at  $z = 0.107$ ), and SN 2015bn (at  $z = 0.1136$ ) are all SLSNe-I that evolved slowly, and could therefore be tracked until very late-times. PS1-14bj was followed-up in the optical but not in the UV, while PTF12dam and SN 2015bn were observed by *Swift* in the UV, but only until 22 days and 120 days after peak, respectively. For PS1-14bj, the blackbody parameters were taken from Lunnan et al. (2016) (derived using the *griz*-bands data). For PTF12dam we show the blackbody parameters from Nicholl et al. (2013). For SN 2015bn, the blackbody parameters are from Nicholl et al. (2016b) (derived using the *UVW2* to *K*-bands fits) until 140 days, and those of Nicholl et al. (2016a) (derived using *u* to *K*-bands fits) for later times. Of these SLSNe-I, both PS1-14bj and SN 2015bn showed undulations in their multi-wavelength light curves.

In Figure 5 we compare the bolometric luminosity evolution. ASASSN-15lh stands out from both the TDEs and SLSNe-I, as it is  $\sim 1$  order of magnitude more luminous than all comparison objects at almost all epochs. Excluding ASASSN-15lh, both classes of transients can have similar peak bolometric luminosities, between  $\sim 1$ – $7 \times 10^{10} L_{\odot}$ . The ASASSN TDEs and most of the SLSNe-I have monotonically dropping luminosities. Only SN 2015bn shows a short plateau (15-day long at  $L \simeq 2.5 \times 10^{10} L_{\odot}$ ), which was also much more pronounced in the UV than in the optical (Nicholl et al. 2016b), resembling ASASSN-15lh.

Figure 6 shows a wide variety of behaviours for the effective temperature of the transients. There is a resemblance between the evolution of ASASSN-15lh and ASASSN-14ae. Besides overlapping temperature values ( $10000 \text{ K} \gtrsim T_{\text{BB}} \gtrsim 20000 \text{ K}$ ), they both decrease in temperature initially, followed by an increase. The timescales, however, are different. While the temperature of ASASSN-15lh starts increasing at



$t \simeq 70$  days, the temperature of ASASSN-14ae starts increasing at  $t \simeq 20$  days.

For SN 2015bn, there is a break in the temperature evolution coincident with the start of the luminosity plateau. It goes from a steady decrease in temperature ( $\sim 11000$  K at  $t \simeq 0$  days), to a 15-day long plateau at  $T_{\text{BB}} \simeq 8500$  K. After this, the effective temperature remains almost constant at  $\sim 7000$  K until very late-times (see also Figure 1 of Nicholl et al. 2016a). PS1-14bj has a very different evolution, showing an effective temperature that increases from  $\sim 7500$  K to  $\sim 10000$  K (even higher temperatures were obtained by Lunnan et al. (2016) using the *riz*-only fits). No clear distinction can be made between TDEs and SLSNe-I based on their effective temperature evolution.

Figure 7 shows that there is a clear distinction between TDEs and SLSNe-I in their photospheric radius evolution. At time of maximum/discovery, the SLSNe-I tend to have larger photospheres than TDEs. This difference increases with time because the photospheric radii of the SLSNe-I shrink much more slowly than those of TDEs. Here, ASASSN-15lh is clearly similar to the SLSNe-I and different from the TDEs, as it remains above  $\sim 10^{15}$  cm for more than  $\sim 450$  days. In fact, blackbody radii of  $\sim 10^{15}$  cm are also typical of other SLSNe-I (e.g. Quimby et al. 2011). Figure 7 shows that ASASSN-14ae and SN 2015bn also have breaks in their photospheric radius evolution. However, once ASASSN-14ae starts shrinking, it evolves much faster. For SN 2015bn the radius evolution break happens simultaneously with the luminosity and temperature plateaus.

Of the TDEs ASASSN-14ae would be the most similar to ASASSN-15lh in temperature and radius evolution, although it is also the least luminous of the three. For the SLSNe-I, SN 2015bn shows a luminosity plateau, and the multi-wavelength light curve at this time has a similar behaviour to what was seen in the *U*-band of ASASSN-15lh after the *valley*.

It is important to note that SLSNe have not been generally observed at UV wavelengths at late-times. When they have been, as in SN 2015bn, the cadence tends to be poor. Figure 1 shows how important UV observations are for energetic transients, as the UV rebrightening of ASASSN-15lh would have been missed without *Swift* observations. Only the *U*-band showed a strong change in its evolution, while the *V* and *B*-bands simply continued to monotonically decline. Therefore, while the rebrightening seen in ASASSN-15lh seems unique, we do not actually have the data to place strong constraints on the existence of similar episodes in SLSNe at late-times. This is different from the ASASSN-TDEs, where the late-time UV data are available.

#### 4.3.2 Spectroscopic Evolution

The spectroscopic features shown by ASASSN-15lh are peculiar among SLSNe, but they are also peculiar among TDEs. The early-time spectroscopy, and in particular the resemblance of the absorption feature at  $\sim 4100$  Å to SN 2010gx, pointed towards the correct redshift of ASASSN-15lh, and was later confirmed by detecting the Mg II absorption doublet at  $2796$  Å and  $2803$  Å (Dong et al. 2016).

Leloudas et al. (2016) agree that the  $\sim 4100$  Å feature is not seen in TDEs, but argue that the absence of the  $\sim 4400$  Å feature in the early spectra of ASASSN-15lh

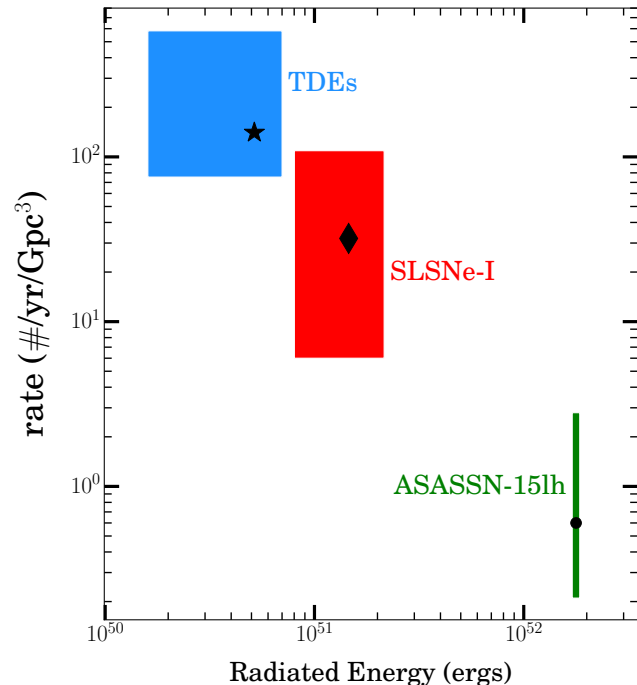


**Figure 8.** Volumetric rate of events as a function of radiated energy for ASASSN-15lh (green), SLSNe-I (red), and TDEs (blue). The typical values are indicated by the black symbols, while the surrounding regions show typical parameters range for each class.

points towards a different physical origin than the O II interpretation for SLSNe-I. In addition, the early-time spectrum of SN 2010gx was reproduced with simple assumptions by Margutti et al. (2016) (see their Figure 6), but this was not the case for ASASSN-15lh, because of the missing  $\sim 4400$  Å absorption feature. The possibility that our initial conjecture of the redshift of ASASSN-15lh, based on the similarities of its early spectra with other SLSNe-I, was only serendipitous, cannot be discarded.

Looking at the overall evolution, Figure 2 shows that the spectrum ASASSN-15lh is always continuum dominated, even at very late-times, without the appearance of nebular features. This differs from what has been seen in SLSNe-I and optically bright TDEs. These TDEs all show prominent He or H+He emission lines soon after peak (e.g., Arcavi et al. 2014; Holoien et al. 2016b,a), while the SLSNe-I stop being continuum dominated well before the time of our latest ASASSN-15lh spectrum (Nicholl et al. 2016b; Lunnan et al. 2016). Although here we do not perform direct comparisons between the spectra of ASASSN-15lh with TDEs and SLSNe, recently Leloudas et al. (2016) carried out such exercise (see their Supplementary Figure 1), showing that similarities and differences arise with both classes of transients, without finding any definitive evidence favouring either class based on their spectra.

#### 4.3.3 Rates and Energies

As a last comparison, Figure 8 shows the rough distribution of TDEs and SLSNe-I as a function of rate and radiated energy. Dong et al. (2016) estimated the rate of ASASSN-15lh-like events to be  $r = 0.60 \text{ yr}^{-1} \text{ Gpc}^{-3}$  ( $0.21 < r < 2.8$ ).

For SLSNe-I, Quimby et al. (2013) estimated the rate to be  $r = 32 \text{ yr}^{-1} \text{ Gpc}^{-3}$  ( $6 < r < 109$ ) (see also Prajs et al. 2016 for a rate at  $z \sim 1$ ). For TDEs, van Velzen & Farrar (2014) estimated the rate to be  $r = (1.5 - 2.0)_{-1.3}^{+2.7} \times 10^{-5} \text{ yr}^{-1} \text{ galaxy}^{-1}$ , corresponding to a volumetric rate of  $r = (4 - 8) \times 10^{1 \pm 0.4} \text{ yr}^{-1} \text{ Gpc}^{-3}$ . The TDE rate estimated by Holoien et al. (2016b),  $r \simeq 4.1 \times 10^{-5} \text{ yr}^{-1} \text{ galaxy}^{-1}$  ( $2.2 < r < 17.0$ ), is higher than that of van Velzen & Farrar (2014), though they are consistent within the uncertainties. The discovery of the third ASAS-SN TDE promptly after the second one lead us to favour the rate estimated by Holoien et al. (2016b). In order to translate this rate per galaxy to a volumetric one, we have followed Kochanek (2016) and scaled it with a constant rate ratio relative to that of van Velzen & Farrar (2014).

We integrated the bolometric luminosity of the objects used in Figures 5–7 using the trapezoidal rule to estimate the radiated energies. For SLSNe-I and TDEs, we have defined the minimum (maximum) of the energy interval to be the energy of the least (most) luminous event within the class, and the representative energy as the average energy of the members. For ASASSN-15lh, we have defined the energy interval using the constant and rising temperature prior at early-times, and the representative energy as the average of those. For ASASSN-14li we adopted the total radiated energy of  $E \simeq 7 \times 10^{50}$  ergs including the X-ray emission reported by Brown et al. (2016b).

Figure 8 shows that events as energetic as ASASSN-15lh are rare among both TDEs and previously identified SLSNe-I, but the stretch from the SLSNe-I to ASASSN-15lh is much less extreme than for the TDEs. It is plausible that ASASSN-15lh is simply an extension of the SLSN distribution as we noted in Dong et al. (2016). Making ASASSN-15lh an extension of the TDE distribution is much more challenging because of the high TDE rates and the absence of TDEs of intermediate energies, in addition to the extreme parameters required under this scenario (see Leloudas et al. 2016).

## 5 SUMMARY

Here we report on the peculiar evolution of ASASSN-15lh. The two most salient features are an extended UV rebrightening phase followed by a renewed fading, and a continued lack of spectroscopic features. The total radiated energy is roughly  $E \simeq 1.7 \times 10^{52}$  ergs, with  $\sim 56\%$  coming from the initial phase and  $\sim 44\%$  from the later plateau and fading phases.

We continue to favor the SLSN-I interpretation of this event over the primary alternative of a TDE. No optically bright TDE to date shows an absence of broad emission lines like ASASSN-15lh. The recent results from Margutti et al. (2016) clearly show that the weak feature we discussed relative to our SOAR *fading* stage spectrum, and the feature interpreted as broad  $H\alpha$  by Leloudas et al. (2016), is actually a blend of narrow  $H\alpha$  and  $[\text{N II}]$  emission, probably due to star formation in the galaxy nucleus.

We also compare the evolution of ASASSN-15lh in luminosity, effective temperature, and photospheric radius to a selection of SLSNe-I and optically bright TDEs. Only the photospheric radius seems to clearly separate the two

classes, and for this parameter ASASSN-15lh behaves like a SLSN-I. The luminosity and temperature evolution provide no strong discrimination between the two classes, possibly due to the lack of good UV data for typical SLSNe. We also note that the radiated energy and the event rate implied by ASASSN-15lh are easier to reconcile with the properties of SLSNe-I than with those of TDEs.

Continued monitoring of ASASSN-15lh will help to address some of these issues. For example, the X-ray emission detected by Margutti et al. (2016) is really only interpretable if it is seen to vary. The most likely route to resolving the riddle of ASASSN-15lh is simply to obtain better population statistics. In particular, larger TDE samples will clarify the range of their evolutionary and spectral properties. Continuous UV observations of SLSNe will clarify whether features like the rebrightening and plateau phases of ASASSN-15lh are ubiquitous in these events, as potentially hinted by SN 2015bn.

## ACKNOWLEDGMENTS

We thank Barry Madore and Juan Carlos Mateos Munoz for obtaining spectra. We thank Matt Nicholl, Cosimo Inserra, Andrea Pastorello, and Ragnhild Lunnan for providing the blackbody parameters of SLSNe, and John Brown for providing the blackbody parameters of ASASSN-14ae. We thank Tuguldur Sukhbold and Tyler Holland-Ashford for useful discussions.

The authors thank LCOGT and its staff for their continued support of ASAS-SN.

We thank Neil Gehrels for approving our various *Swift* ToO requests and the *Swift* science operation team for performing the observations. This research has made use of the XRT Data Analysis Software (XRTDAS) developed under the responsibility of the ASI Science Data Center (ASDC), Italy. This research has made use of data obtained through the High Energy Astrophysics Science Archive Research Center Online Service, provided by the NASA/Goddard Space Flight Center.

ASAS-SN is supported by NSF grant AST-1515927. Development of ASAS-SN has been supported by NSF grant AST-0908816, the Center for Cosmology and AstroParticle Physics at the Ohio State University, the Mt. Cuba Astronomical Foundation, and by George Skestos.

DGR is supported by The Ohio State University through the Dean’s Distinguished University Fellowship. PC and SD are supported by “the Strategic Priority Research Program-The Emergence of Cosmological Structures” of the Chinese Academy of Sciences (Grant No. XDB09000000) and Project 11573003 supported by NSFC. This research uses data obtained through the Telescope Access Program (TAP), which has been funded by “the Strategic Priority Research Program- The Emergence of Cosmological Structures” of the Chinese Academy of Sciences (Grant No.11 XDB09000000) and the Special Fund for Astronomy from the Ministry of Finance. Support for JLP is in part provided by FONDECYT through the grant 1151445 and by the Ministry of Economy, Development, and Tourism’s Millennium Science Initiative through grant IC120009, awarded to The Millennium Institute of Astrophysics, MAS. BJS is supported by NASA through Hubble Fellowship grant HF-

51348.001 awarded by the Space Telescope Science Institute, which is operated by the Association of Universities for Research in Astronomy, Inc., for NASA, under contract NAS 5-26555. The UCSC group is supported in part by NSF grant AST-1518052 and from fellowships from the Alfred P. Sloan Foundation and the David and Lucile Packard Foundation to R.J.F. TW-SH is supported by the DOE Computational Science Graduate Fellowship, grant number DE-FG02-97ER25308. JFB is supported by NSF grant PHY-1404311.

This paper includes data gathered with the 6.5 meter Magellan Telescopes located at Las Campanas Observatory, Chile.

## REFERENCES

- Arcavi I. et al., 2014, *ApJ*, 793, 38  
 Arcavi I. et al., 2016, *ApJ*, 819, 35  
 Breeveld A. A. et al., 2010, *MNRAS*, 406, 1687  
 Brown J. S., Shappee B. J., Holoiën T. W.-S., Stanek K. Z., Kochanek C. S., Prieto J. L., 2016a, *MNRAS*, 462, 3993  
 Brown J. S., W.-S Holoiën T., Auchtell K., Stanek K. Z., Kochanek C. S., Shappee B. J., Prieto J. L., Grupe D., 2016b, *ArXiv e-prints*, arXiv:1609.04403  
 Brown P. J., 2015, *The Astronomer’s Telegram*, 8086  
 Brown P. J. et al., 2016c, *ApJ*, 828, 3  
 Brown T. M. et al., 2013, *PASP*, 125, 1031  
 Burrows D. N. et al., 2005, *Space Sci. Rev.*, 120, 165  
 Chatzopoulos E., Wheeler J. C., Vinko J., Horvath Z. L., Nagy A., 2013, *ApJ*, 773, 76  
 Chatzopoulos E., Wheeler J. C., Vinko J., Nagy A. P., Wiggins B. K., Even W. P., 2016, *ApJ*, 828, 94  
 Chen T.-W. et al., 2015, *MNRAS*, 452, 1567  
 Chevalier R. A., Irwin C. M., 2011, *ApJL*, 729, L6  
 Clemens J. C., Crain J. A., Anderson R., 2004, in *Society of Photo-Optical Instrumentation Engineers (SPIE) Conference Series*, Vol. 5492, *Ground-based Instrumentation for Astronomy*, Moorwood A. F. M., Iye M., eds., pp. 331–340  
 Crawford S. M. et al., 2010, in *Society of Photo-Optical Instrumentation Engineers (SPIE) Conference Series*, Vol. 7737, *Society of Photo-Optical Instrumentation Engineers (SPIE) Conference Series*, p. 25  
 Dong S. et al., 2016, *Science*, 351, 257  
 Foley R. J. et al., 2003, *PASP*, 115, 1220  
 Gal-Yam A., 2012, *Science*, 337, 927  
 Gal-Yam A. et al., 2009, *Nature*, 462, 624  
 Ginzburg S., Balberg S., 2012, *ApJ*, 757, 178  
 Henden A. A., Levine S., Terrell D., Welch D. L., 2015, in *American Astronomical Society Meeting Abstracts*, Vol. 225, *American Astronomical Society Meeting Abstracts*, p. 336.16  
 Hill J. E. et al., 2004, in *SPIE Conference Series*, Vol. 5165, *X-Ray and Gamma-Ray Instrumentation for Astronomy XIII*, Flanagan K. A., Siegmund O. H. W., eds., pp. 217–231  
 Holoiën T. W.-S. et al., 2016a, *MNRAS*  
 Holoiën T. W.-S. et al., 2016b, *MNRAS*, 455, 2918  
 Holoiën T. W.-S. et al., 2014, *MNRAS*, 445, 3263  
 Horne K., 1986, *PASP*, 98, 609  
 Inserra C. et al., 2016, *ArXiv e-prints*, arXiv:1604.01226  
 Inserra C. et al., 2013, *ApJ*, 770, 128  
 Kaiser N. et al., 2002, in *Proc. SPIE*, Vol. 4836, *Survey and Other Telescope Technologies and Discoveries*, Tyson J. A., Wolff S., eds., pp. 154–164  
 Kasen D., Bildsten L., 2010, *ApJ*, 717, 245  
 Kochanek C. S., 2016, *MNRAS*, 461, 371  
 Kool E. C., Ryder S. D., Stockdale C. J., Romero-Canizales C., Prieto J. L., Kotak R., 2015, *The Astronomer’s Telegram*, 8388  
 Kozyreva A., Hirschi R., Blinnikov S., den Hartogh J., 2016, *MNRAS*, 459, L21  
 Kraft R. P., Burrows D. N., Nousek J. A., 1991, *ApJ*, 374, 344  
 Law N. M. et al., 2009, *PASP*, 121, 1395  
 Leloudas G. et al., 2016, *ArXiv e-prints*, arXiv:1609.02927  
 Lunnan R. et al., 2016, *ApJ*, 831, 144  
 Lunnan R. et al., 2015, *ApJ*, 804, 90  
 Maddox S. J., Efstathiou G., Sutherland W. J., Loveday J., 1990, *MNRAS*, 243, 692  
 Margutti R. et al., 2016, *ArXiv e-prints*, arXiv:1610.01632  
 Marshall J. L. et al., 2008, in *Proc. SPIE*, Vol. 7014, *Ground-based and Airborne Instrumentation for Astronomy II*, p. 701454  
 Metzger B. D., Margalit B., Kasen D., Quataert E., 2015, *MNRAS*, 454, 3311  
 Metzger B. D., Vurm I., Hascoët R., Beloborodov A. M., 2014, *MNRAS*, 437, 703  
 Milisavljevic D., James D. J., Marshall J. L., Patnaude D., Margutti R., Parrent J., Kamble A., 2015, *The Astronomer’s Telegram*, 8216  
 Neill J. D. et al., 2011, *ApJ*, 727, 15  
 Nicholl M. et al., 2016a, *ApJL*, 828, L18  
 Nicholl M. et al., 2016b, *ApJ*, 826, 39  
 Nicholl M. et al., 2013, *Nature*, 502, 346  
 Pastorello A. et al., 2010, *ApJL*, 724, L16  
 Poole T. S. et al., 2008, *MNRAS*, 383, 627  
 Prajs S. et al., 2016, *MNRAS*  
 Quimby R. M., 2006, PhD thesis, The University of Texas at Austin  
 Quimby R. M. et al., 2011, *Nature*, 474, 487  
 Quimby R. M., Yuan F., Akerlof C., Wheeler J. C., 2013, *MNRAS*, 431, 912  
 Rau A. et al., 2009, *PASP*, 121, 1334  
 Roming P. W. A. et al., 2005, *Space Sci. Rev.*, 120, 95  
 Schlafly E. F., Finkbeiner D. P., 2011, *ApJ*, 737, 103  
 Shappee B. J. et al., 2014, *ApJ*, 788, 48  
 Silverman J. M. et al., 2012, *MNRAS*, 425, 1789  
 Smith M. P., Nordsieck K. H., Burgh E. B., Percival J. W., Williams T. B., O’Donohue D., O’Connor J., Schier J. A., 2006, in *Society of Photo-Optical Instrumentation Engineers (SPIE) Conference Series*, Vol. 6269, p. 62692A  
 Sorokina E., Blinnikov S., Nomoto K., Quimby R., Tolstov A., 2016, *ApJ*, 829, 17  
 Stoll R., Prieto J. L., Stanek K. Z., Pogge R. W., Szczygiel D. M., Pojmański G., Antognini J., Yan H., 2011, *ApJ*, 730, 34  
 Sukhbold T., Woosley S. E., 2016, *ApJL*, 820, L38  
 van Velzen S., Farrar G. R., 2014, *ApJ*, 792, 53  
 Wade R. A., Horne K., 1988, *ApJ*, 324, 411  
 Wang S. Q., Liu L. D., Dai Z. G., Wang L. J., Wu X. F., 2016, *ApJ*, 828, 87  
 Woosley S. E., 2010, *ApJL*, 719, L204

Yan L. et al., 2015, ApJ, 814, 108

Young D. R. et al., 2010, AAP, 512, A70

Table 1. *Swift* photometric data of ASASSN-15lh.

MJD	<i>UVW2</i>	$\sigma_{UVW2}$	<i>UVM2</i>	$\sigma_{UVM2}$	<i>UVW1</i>	$\sigma_{UVW1}$	<i>U</i>	$\sigma_U$	<i>B</i>	$\sigma_B$	<i>V</i>	$\sigma_V$
57197.0	15.46	0.05	15.15	0.06	15.20	0.05	15.38	0.04	16.76	0.06	17.05	0.14
57199.8	15.55	0.05	15.22	0.05	15.22	0.05	15.44	0.04	16.75	0.05	16.76	0.10
57201.8	15.83	0.05	15.48	0.06	15.32	0.05	15.51	0.05	16.89	0.06	16.96	0.13
57205.5	15.76	0.05	15.51	0.05	15.47	0.05	15.59	0.05	16.97	0.06	16.92	0.11
57208.6	15.95	0.07	15.69	0.06	15.58	0.07	15.83	0.07	17.04	0.09	16.89	0.17
57211.5	16.20	0.07	15.87	0.06	15.81	0.07	15.74	0.07	17.10	0.09	17.05	0.16
57214.6	16.18	0.05	15.94	0.07	15.81	0.06	15.86	0.05	17.14	0.06	17.12	0.12
57214.7	16.28	0.07	16.04	0.07	15.89	0.07	15.89	0.07	17.03	0.08	17.31	0.19
57216.4	16.42	0.09	-	-	-	-	15.91	0.04	-	-	-	-
57216.5	-	-	-	-	-	-	15.87	0.04	-	-	-	-
57216.8	-	-	-	-	-	-	15.90	0.04	-	-	-	-
57217.1	16.30	0.05	-	-	-	-	-	-	-	-	-	-
57217.6	16.30	0.07	-	-	-	-	-	-	-	-	-	-
57219.7	16.47	0.10	-	-	16.18	0.06	-	-	-	-	-	-
57220.5	16.63	0.09	-	-	-	-	16.08	0.04	-	-	-	-
57221.7	16.57	0.06	16.42	0.06	16.22	0.06	16.03	0.05	17.29	0.07	17.28	0.13
57223.5	16.73	0.06	16.60	0.06	16.32	0.06	16.17	0.06	17.37	0.07	17.24	0.13
57226.1	17.00	0.09	16.71	0.10	16.46	0.09	16.28	0.07	17.39	0.09	17.12	0.15
57229.1	17.24	0.11	16.82	0.10	16.58	0.10	16.61	0.12	17.34	0.12	17.50	0.26
57232.8	17.34	0.09	17.17	0.09	16.84	0.09	16.42	0.08	17.51	0.10	17.53	0.20
57241.1	17.70	0.09	17.48	0.08	17.13	0.08	16.66	0.07	17.56	0.08	17.65	0.16
57244.9	17.80	0.10	17.63	0.09	17.40	0.10	16.77	0.08	17.72	0.09	17.50	0.16
57248.4	17.96	0.10	17.67	0.10	17.38	0.10	16.76	0.09	17.60	0.10	17.66	0.20
57250.7	17.93	0.10	17.71	0.10	17.22	0.10	16.82	0.09	17.51	0.09	17.34	0.16
57253.6	17.96	0.13	17.67	0.12	17.27	0.13	16.62	0.10	17.69	0.12	17.37	0.21
57255.6	18.08	0.10	17.89	0.13	17.41	0.10	16.88	0.07	17.77	0.08	17.87	0.18
57259.3	18.43	0.16	17.94	0.13	17.43	0.13	17.05	0.12	17.95	0.14	17.78	0.27
57262.6	18.19	0.16	18.01	0.14	17.38	0.13	17.03	0.13	17.83	0.14	17.57	0.25
57265.5	18.76	0.33	-	-	17.42	0.10	16.99	0.09	17.97	0.11	-	-
57268.7	18.30	0.12	17.96	0.10	17.52	0.10	17.02	0.09	17.83	0.10	17.55	0.17
57272.4	18.23	0.12	17.78	0.13	17.26	0.10	16.88	0.08	17.87	0.10	17.57	0.16
57272.8	18.00	0.10	17.88	0.16	17.43	0.10	16.99	0.09	17.85	0.11	17.62	0.19
57277.3	17.70	0.08	17.57	0.10	17.05	0.08	16.88	0.06	17.74	0.07	17.51	0.11
57282.8	17.60	0.10	17.51	0.13	17.09	0.10	16.91	0.09	-	-	-	-
57283.1	17.79	0.10	17.14	0.11	17.18	0.10	17.01	0.09	-	-	-	-
57284.2	17.60	0.10	17.26	0.09	17.09	0.10	16.98	0.10	17.85	0.12	17.91	0.25
57284.6	17.66	0.10	17.29	0.12	17.04	0.10	16.85	0.09	17.89	0.11	18.13	0.26
57290.8	17.60	0.09	17.23	0.10	17.06	0.09	16.87	0.07	-	-	-	-
57293.5	17.46	0.07	16.95	0.07	16.92	0.07	16.99	0.06	-	-	-	-
57296.5	17.39	0.08	16.87	0.08	16.78	0.08	17.00	0.07	-	-	-	-
57298.6	17.27	0.07	16.96	0.06	16.89	0.08	16.94	0.07	18.10	0.10	17.73	0.16
57299.4	17.34	0.08	16.89	0.09	16.80	0.09	16.90	0.08	-	-	-	-
57302.4	17.46	0.10	17.15	0.13	17.01	0.11	17.07	0.11	-	-	-	-
57305.4	17.13	0.06	17.04	0.08	16.77	0.07	16.88	0.06	17.97	0.08	17.77	0.14
57307.4	17.15	0.07	16.84	0.06	16.82	0.07	16.92	0.08	18.06	0.10	18.07	0.21
57309.7	17.17	0.07	16.85	0.06	16.72	0.08	16.84	0.08	18.29	0.13	17.52	0.15
57311.3	17.01	0.07	16.75	0.06	16.78	0.08	17.04	0.09	18.17	0.12	17.66	0.17
57313.1	17.13	0.10	16.81	0.08	16.74	0.10	16.96	0.12	18.11	0.16	17.94	0.30
57316.2	17.13	0.09	16.94	0.11	16.70	0.10	16.77	0.09	-	-	-	-
57319.7	17.26	0.07	17.02	0.09	16.88	0.08	16.95	0.07	-	-	-	-
57322.7	-	-	17.02	0.09	16.71	0.12	-	-	-	-	-	-
57325.3	17.39	0.06	17.11	0.08	16.89	0.07	16.94	0.06	-	-	-	-
57328.3	17.24	0.10	16.79	0.11	16.84	0.11	16.74	0.11	-	-	-	-
57331.0	17.19	0.08	16.87	0.09	16.84	0.09	16.88	0.08	-	-	-	-
57334.5	17.12	0.07	16.86	0.09	16.75	0.08	16.94	0.08	-	-	-	-

MJD	UVW2	$\sigma_{UVW2}$	UVM2	$\sigma_{UVM2}$	UVW1	$\sigma_{UVW1}$	U	$\sigma_U$	B	$\sigma_B$	V	$\sigma_V$
57343.4	17.18	0.07	16.94	0.08	16.85	0.07	17.00	0.06	-	-	-	-
57349.2	17.10	0.07	16.82	0.08	16.79	0.08	17.06	0.07	-	-	-	-
57353.5	17.16	0.10	16.86	0.10	16.85	0.09	16.93	0.13	-	-	-	-
57356.2	17.03	0.06	-	-	16.92	0.08	16.96	0.07	-	-	-	-
57359.3	17.14	0.07	16.98	0.09	16.90	0.08	16.86	0.07	-	-	-	-
57362.2	17.00	0.12	16.95	0.15	16.73	0.13	17.20	0.18	-	-	-	-
57366.4	17.12	0.17	-	-	17.06	0.21	17.15	0.11	18.31	0.19	-	-
57368.9	17.16	0.08	17.31	0.11	16.87	0.09	17.03	0.09	-	-	-	-
57371.4	17.28	0.07	17.06	0.10	17.15	0.09	17.21	0.08	18.40	0.13	-	-
57374.4	17.36	0.07	16.98	0.09	17.11	0.09	17.22	0.09	-	-	-	-
57377.2	17.30	0.06	17.11	0.08	17.29	0.10	17.30	0.09	-	-	-	-
57380.9	17.36	0.09	16.98	0.10	17.12	0.10	17.24	0.12	-	-	-	-
57383.2	17.42	0.10	17.43	0.19	17.18	0.12	17.29	0.15	-	-	-	-
57385.9	17.31	0.11	17.14	0.15	17.14	0.15	17.19	0.19	-	-	-	-
57393.3	17.35	0.11	17.21	0.19	17.40	0.17	17.09	0.15	-	-	-	-
57396.7	17.67	0.08	17.34	0.09	17.36	0.10	17.34	0.10	18.46	0.16	18.14	0.22
57399.2	17.47	0.08	17.47	0.10	17.42	0.10	17.34	0.11	-	-	18.08	0.25
57427.7	17.95	0.11	17.70	0.12	17.63	0.14	17.74	0.17	18.69	0.26	-	-
57429.4	17.90	0.15	17.53	0.15	17.82	0.22	17.99	0.29	18.26	0.26	-	-
57433.1	18.27	0.19	18.07	0.20	17.59	0.19	17.90	0.31	-	-	-	-
57437.1	17.92	0.10	17.97	0.24	17.56	0.12	17.68	0.15	18.53	0.23	-	-
57447.2	18.04	0.13	17.96	0.16	17.74	0.17	17.75	0.21	-	-	-	-
57449.9	18.18	0.12	17.94	0.14	17.95	0.16	17.73	0.19	-	-	-	-
57450.2	18.20	0.12	18.14	0.16	18.03	0.17	17.65	0.17	18.67	0.27	-	-
57453.9	17.92	0.11	17.91	0.14	17.64	0.14	17.71	0.18	18.57	0.27	-	-
57456.0	17.96	0.10	17.88	0.14	17.81	0.13	18.05	0.18	18.72	0.22	-	-
57457.5	18.37	0.18	-	-	18.10	0.21	17.65	0.18	18.79	0.31	-	-
57465.1	18.16	0.14	18.17	0.20	17.94	0.18	17.83	0.19	-	-	-	-
57470.2	18.15	0.10	17.89	0.11	17.89	0.11	17.69	0.10	-	-	-	-
57472.2	18.19	0.13	18.04	0.16	17.84	0.15	17.76	0.15	19.02	0.27	18.18	0.33
57475.6	18.21	0.11	17.90	0.13	17.88	0.13	17.86	0.13	-	-	-	-
57477.2	18.37	0.18	17.91	0.19	18.03	0.22	17.68	0.21	18.59	0.29	-	-
57480.0	18.45	0.14	18.16	0.16	18.12	0.17	18.06	0.21	-	-	-	-
57487.1	18.44	0.18	18.33	0.23	17.84	0.18	18.00	0.25	-	-	-	-
57489.0	18.30	0.10	18.26	0.13	18.27	0.13	18.00	0.13	-	-	-	-
57499.7	-	-	18.48	0.16	18.35	0.27	-	-	-	-	-	-
57502.7	18.42	0.13	18.21	0.16	18.02	0.16	18.03	0.20	-	-	-	-
57505.2	18.45	0.14	18.39	0.19	17.89	0.15	18.00	0.18	-	-	-	-
57508.9	18.41	0.11	18.27	0.14	17.92	0.12	17.77	0.12	-	-	-	-
57511.8	18.49	0.11	18.46	0.14	18.12	0.12	18.19	0.15	-	-	-	-
57515.9	18.51	0.11	18.37	0.14	18.07	0.11	18.05	0.11	-	-	-	-
57516.3	18.38	0.15	18.20	0.18	18.24	0.19	17.82	0.18	-	-	-	-
57520.3	18.70	0.19	18.38	0.21	18.15	0.19	18.42	0.30	-	-	-	-
57523.7	18.42	0.13	18.45	0.19	18.27	0.17	18.24	0.16	-	-	-	-
57527.9	18.40	0.13	18.33	0.17	18.14	0.16	18.52	0.25	-	-	-	-
57528.9	18.92	0.21	18.71	0.25	18.38	0.22	18.22	0.24	-	-	-	-
57533.6	18.72	0.25	19.17	0.30	18.09	0.22	18.43	0.33	18.77	0.30	-	-
57552.5	18.58	0.18	18.35	0.15	18.89	0.27	18.58	0.28	18.95	0.26	-	-
57554.8	18.64	0.18	18.44	0.16	18.62	0.23	18.25	0.22	-	-	18.01	0.29
57557.2	18.86	0.18	18.56	0.15	18.61	0.20	18.40	0.22	19.38	0.31	-	-
57560.0	18.67	0.13	18.51	0.13	18.44	0.14	18.24	0.16	19.33	0.24	18.63	0.32
57563.0	18.63	0.18	18.39	0.15	18.59	0.24	18.15	0.22	19.15	0.31	-	-
57569.1	18.89	0.23	18.84	0.22	18.11	0.18	18.17	0.23	-	-	18.10	0.35
57577.8	18.86	0.19	18.53	0.22	18.12	0.17	18.45	0.21	-	-	-	-
57591.7	19.29	0.22	19.01	0.27	18.94	0.26	18.40	0.19	-	-	-	-
57600.4	18.90	0.17	19.05	0.24	18.87	0.22	18.50	0.18	-	-	-	-



MJD	<i>UVW2</i>	$\sigma_{UVW2}$	<i>UVM2</i>	$\sigma_{UVM2}$	<i>UVW1</i>	$\sigma_{UVW1}$	<i>U</i>	$\sigma_U$	<i>B</i>	$\sigma_B$	<i>V</i>	$\sigma_V$
57601.4	19.26	0.21	19.13	0.25	18.99	0.23	18.53	0.18	-	-	-	-
57608.0	19.33	0.32	18.73	0.25	18.60	0.24	18.85	0.33	-	-	-	-
57609.0	19.01	0.16	19.16	0.23	18.59	0.16	18.57	0.17	-	-	-	-
57611.5	19.27	0.17	18.90	0.19	19.13	0.22	18.86	0.20	-	-	-	-
57615.4	18.94	0.12	18.87	0.16	18.72	0.15	18.79	0.16	-	-	-	-
57622.5	19.16	0.26	-	-	18.76	0.20	18.70	0.15	-	-	-	-
57626.7	19.38	0.23	19.42	0.36	18.96	0.28	-	-	-	-	-	-
57630.4	19.03	0.23	-	-	-	-	18.50	0.26	-	-	-	-
57632.8	18.92	0.20	-	-	-	-	18.86	0.28	-	-	-	-
57640.0	19.58	0.26	19.13	0.26	18.89	0.25	18.65	0.20	-	-	-	-
57645.5	19.56	0.24	19.36	0.32	18.76	0.23	18.78	0.24	-	-	-	-
57654.2	19.35	0.32	-	-	18.64	0.31	18.73	0.34	-	-	-	-
57667.3	19.31	0.31	-	-	-	-	-	-	-	-	-	-
57677.3	19.37	0.32	-	-	-	-	-	-	-	-	-	-
57680.2	19.21	0.30	-	-	18.72	0.36	-	-	-	-	-	-
57682.5	19.32	0.15	19.36	0.23	19.13	0.20	19.11	0.21	-	-	-	-
57687.0	19.19	0.24	-	-	-	-	-	-	-	-	-	-
57688.9	19.31	0.25	18.92	0.31	-	-	19.06	0.36	-	-	-	-
57704.0	19.93	0.33	-	-	-	-	18.85	0.27	-	-	-	-

**Table 2.** LCOGT photometric data of ASASSN-15lh.

MJD	$B$	$\sigma_B$	$V$	$\sigma_V$
57190.4	16.78	0.07	16.84	0.04
57196.1	16.75	0.03	16.85	0.03
57196.2	16.72	0.03	16.90	0.03
57200.8	16.86	0.05	16.91	0.04
57203.1	16.83	0.05	16.97	0.04
57204.2	16.86	0.04	16.96	0.04
57206.2	16.88	0.05	17.02	0.05
57208.6	16.92	0.08	17.06	0.04
57210.3	16.95	0.05	-	-
57212.5	17.07	0.04	17.13	0.04
57216.9	17.06	0.05	17.14	0.06
57219.0	17.11	0.03	17.24	0.04
57221.2	17.29	0.04	17.30	0.03
57222.9	17.25	0.04	17.35	0.05
57225.4	17.38	0.07	-	-
57227.3	17.34	0.07	-	-
57228.7	17.33	0.06	-	-
57230.5	17.36	0.07	-	-
57234.5	17.50	0.08	-	-
57240.0	17.59	0.05	17.48	0.04
57241.0	17.51	0.04	17.48	0.04
57242.5	17.58	0.05	17.49	0.04
57244.5	-	-	17.55	0.04
57245.4	17.60	0.04	17.55	0.04
57247.5	17.72	0.04	17.52	0.04
57250.5	17.63	0.04	17.61	0.04
57253.5	17.66	0.03	17.56	0.04
57256.6	-	-	17.65	0.05
57258.0	17.79	0.08	-	-
57261.1	17.79	0.05	17.66	0.05
57262.3	17.99	0.09	-	-
57262.6	17.88	0.07	17.66	0.07
57264.1	17.99	0.08	17.65	0.06
57267.2	17.90	0.05	17.68	0.04
57268.1	17.87	0.05	17.73	0.03
57270.2	17.90	0.05	-	-
57274.0	-	-	17.70	0.04
57279.0	17.89	0.07	17.66	0.05
57282.3	17.93	0.05	17.75	0.03
57285.0	-	-	17.88	0.06
57286.0	17.95	0.04	17.76	0.04
57288.3	17.90	0.05	17.68	0.04
57288.6	17.85	0.05	17.78	0.04
57291.1	17.96	0.06	17.82	0.05
57296.5	18.01	0.05	17.79	0.04
57298.6	17.92	0.08	17.84	0.04
57301.5	-	-	17.81	0.04
57302.9	17.97	0.04	17.79	0.04
57304.5	17.98	0.04	-	-
57305.5	17.92	0.04	17.81	0.03
57307.9	18.01	0.05	17.83	0.04
57311.0	17.96	0.04	17.81	0.04
57319.8	17.90	0.06	17.92	0.06
57328.8	18.01	0.05	17.87	0.04
57332.1	18.03	0.05	17.86	0.03

MJD	$B$	$\sigma_B$	$V$	$\sigma_V$
57334.8	18.04	0.05	17.87	0.03
57338.1	18.13	0.05	17.88	0.03
57345.5	18.14	0.06	18.02	0.05
57350.8	18.06	0.06	17.94	0.05
57353.8	18.12	0.05	17.95	0.04
57356.8	18.12	0.04	17.97	0.04
57360.5	18.27	0.04	18.04	0.03
57363.0	18.17	0.08	18.02	0.03
57366.8	18.23	0.04	18.05	0.04
57373.1	18.27	0.05	18.06	0.03
57375.4	18.29	0.05	18.08	0.04
57378.0	-	-	18.10	0.04
57379.0	-	-	18.13	0.04
57492.1	-	-	18.50	0.05
57563.4	19.03	0.08	18.61	0.06
57581.2	-	-	18.63	0.06
57587.1	19.28	0.10	18.59	0.06
57598.4	-	-	18.69	0.05
57598.7	19.37	0.09	18.75	0.06
57598.8	19.44	0.09	-	-
57602.1	-	-	18.53	0.05
57607.2	19.58	0.07	18.69	0.11
57612.8	-	-	18.71	0.06
57613.7	19.46	0.08	-	-
57624.0	19.52	0.11	18.75	0.06
57634.2	-	-	18.77	0.05
57637.9	19.60	0.09	18.76	0.05
57643.3	19.56	0.09	18.84	0.05
57654.3	-	-	18.74	0.06
57663.2	-	-	18.80	0.05
57668.1	19.51	0.08	18.75	0.06
57670.2	19.51	0.09	18.83	0.06
57672.8	19.44	0.20	-	-
57680.1	-	-	18.73	0.06
57687.6	-	-	18.77	0.06
57687.9	19.61	0.07	18.77	0.05
57694.5	19.76	0.07	18.85	0.05
57699.9	19.57	0.08	-	-

**Table 3.** Blackbody models for the bolometric luminosity, effective temperature, and apparent photospheric radius of ASASSN-15lh using the constant-temperature prior for early-times ( $t < 12.5$  days). The units of the variables are solar luminosities, Kelvin, and centimeters, respectively. The logarithms are all in base 10.

MJD	$N_{\text{obs}}$	$\log(L)$	$\log(L_-)$	$\log(L_+)$	$\log(T)$	$\log(T_-)$	$\log(T_+)$	$\log(R)$	$\log(R_-)$	$\log(R_+)$
57150.5	1	11.43	11.26	11.62	4.32	4.24	4.40	15.45	15.36	15.54
57157.0	1	11.27	11.09	11.45	4.32	4.24	4.40	15.36	15.27	15.45
57161.1	1	11.53	11.36	11.73	4.32	4.24	4.40	15.50	15.41	15.59
57169.8	1	11.75	11.58	11.93	4.32	4.24	4.40	15.60	15.52	15.69
57172.7	1	11.64	11.47	11.83	4.32	4.24	4.40	15.55	15.46	15.64
57181.8	1	11.75	11.58	11.94	4.32	4.24	4.40	15.60	15.52	15.70
57184.0	1	11.66	11.49	11.85	4.32	4.24	4.40	15.56	15.47	15.65
57190.7	2	11.61	11.44	11.79	4.32	4.24	4.40	15.53	15.45	15.62

**Table 4.** Blackbody models for the bolometric luminosity, effective temperature, and apparent photospheric radius of ASASSN-15lh using the rising-temperature prior for early-times ( $t < 12.5$  days). The units of the variables are solar luminosities, Kelvin, and centimeters, respectively. The logarithms are all in base 10.

MJD	$N_{\text{obs}}$	$\log(L)$	$\log(L_-)$	$\log(L_+)$	$\log(T)$	$\log(T_-)$	$\log(T_+)$	$\log(R)$	$\log(R_-)$	$\log(R_+)$
57150.5	1	11.69	11.50	11.89	4.44	4.36	4.52	15.34	15.26	15.42
57157.0	1	11.49	11.30	11.69	4.42	4.34	4.51	15.27	15.19	15.35
57161.1	1	11.73	11.54	11.93	4.41	4.33	4.49	15.41	15.33	15.50
57169.8	1	11.89	11.71	12.09	4.39	4.31	4.47	15.54	15.46	15.62
57172.7	1	11.77	11.58	11.96	4.38	4.30	4.46	15.49	15.41	15.58
57181.8	1	11.81	11.64	12.00	4.35	4.27	4.43	15.57	15.49	15.66
57184.0	1	11.71	11.53	11.90	4.34	4.26	4.43	15.54	15.45	15.63
57190.7	2	11.61	11.44	11.79	4.32	4.24	4.41	15.53	15.45	15.62

**Table 5.** Blackbody models for the bolometric luminosity, effective temperature, and apparent photospheric radius of ASASSN-15lh for times after  $t = 12.5$  days, when no prior is required. The units of the variables are solar luminosities, Kelvin, and centimeters, respectively. The logarithms are all in base 10.

MJD	$N_{\text{obs}}$	$\log(L)$	$\log(L_-)$	$\log(L_+)$	$\log(T)$	$\log(T_-)$	$\log(T_+)$	$\log(R)$	$\log(R_-)$	$\log(R_+)$
57197.0	6	11.79	11.75	11.84	4.32	4.28	4.35	15.63	15.57	15.69
57199.8	6	11.76	11.73	11.80	4.27	4.24	4.30	15.72	15.66	15.77
57201.8	6	11.68	11.65	11.71	4.25	4.22	4.29	15.70	15.65	15.76
57205.5	6	11.67	11.63	11.70	4.26	4.23	4.29	15.69	15.63	15.75
57208.6	6	11.61	11.57	11.64	4.23	4.21	4.26	15.71	15.65	15.76
57211.5	6	11.54	11.51	11.58	4.21	4.18	4.24	15.72	15.66	15.77
57214.7	6	11.52	11.48	11.55	4.22	4.19	4.25	15.69	15.63	15.75
57221.7	6	11.40	11.37	11.43	4.18	4.16	4.21	15.71	15.65	15.76
57223.5	6	11.36	11.33	11.39	4.16	4.14	4.19	15.73	15.67	15.78
57226.1	6	11.34	11.31	11.37	4.13	4.11	4.15	15.78	15.73	15.84
57229.1	6	11.25	11.22	11.28	4.14	4.12	4.17	15.71	15.66	15.77
57232.8	6	11.21	11.18	11.24	4.12	4.10	4.14	15.74	15.68	15.79
57241.1	6	11.13	11.10	11.17	4.09	4.07	4.12	15.75	15.70	15.80
57244.9	6	11.11	11.08	11.15	4.07	4.05	4.09	15.78	15.73	15.83
57248.4	6	11.10	11.06	11.14	4.07	4.05	4.09	15.78	15.73	15.83
57250.7	6	11.17	11.13	11.21	4.05	4.03	4.07	15.86	15.81	15.91
57253.6	6	11.16	11.12	11.20	4.05	4.03	4.07	15.85	15.80	15.90
57255.6	6	11.02	10.98	11.06	4.08	4.06	4.10	15.72	15.67	15.77
57259.3	6	11.00	10.96	11.04	4.06	4.04	4.08	15.75	15.70	15.80
57262.6	6	11.06	11.02	11.10	4.05	4.03	4.07	15.80	15.75	15.85
57268.7	6	11.06	11.02	11.10	4.04	4.02	4.06	15.82	15.76	15.87
57272.6	6	11.06	11.03	11.10	4.07	4.05	4.08	15.77	15.72	15.82
57277.3	6	11.12	11.08	11.15	4.09	4.07	4.11	15.74	15.69	15.80
57282.9	6	11.06	11.03	11.10	4.13	4.11	4.16	15.63	15.58	15.69
57284.4	6	11.04	11.01	11.07	4.17	4.14	4.20	15.55	15.49	15.60
57290.8	6	11.07	11.04	11.10	4.15	4.13	4.17	15.61	15.55	15.66
57293.5	6	11.10	11.06	11.13	4.18	4.16	4.21	15.55	15.50	15.61
57296.5	6	11.12	11.08	11.15	4.20	4.17	4.22	15.54	15.48	15.59
57299.0	6	11.11	11.08	11.14	4.20	4.17	4.23	15.53	15.47	15.58
57302.4	6	11.07	11.04	11.11	4.17	4.14	4.20	15.57	15.51	15.62
57305.4	6	11.13	11.10	11.16	4.21	4.18	4.23	15.53	15.47	15.58
57307.4	6	11.12	11.09	11.16	4.26	4.23	4.30	15.40	15.34	15.46
57309.7	6	11.15	11.12	11.18	4.21	4.18	4.23	15.53	15.48	15.59
57311.3	6	11.15	11.12	11.19	4.24	4.21	4.27	15.47	15.41	15.53
57313.1	6	11.13	11.10	11.17	4.25	4.22	4.29	15.43	15.37	15.48
57316.2	6	11.15	11.12	11.18	4.21	4.19	4.24	15.52	15.46	15.57
57319.7	6	11.11	11.07	11.14	4.20	4.18	4.23	15.52	15.46	15.57
57325.3	6	11.09	11.06	11.12	4.19	4.16	4.21	15.54	15.48	15.59
57328.3	6	11.14	11.11	11.17	4.21	4.19	4.24	15.51	15.45	15.57
57331.0	6	11.13	11.10	11.16	4.22	4.19	4.25	15.50	15.44	15.55
57334.5	6	11.14	11.11	11.17	4.23	4.20	4.26	15.47	15.42	15.53
57343.4	6	11.10	11.07	11.13	4.24	4.21	4.27	15.44	15.38	15.49
57349.2	6	11.13	11.09	11.16	4.25	4.22	4.29	15.42	15.37	15.48
57353.5	6	11.12	11.09	11.15	4.24	4.21	4.27	15.45	15.39	15.50
57359.3	6	11.10	11.07	11.13	4.25	4.22	4.28	15.42	15.37	15.48
57362.2	6	11.12	11.08	11.16	4.28	4.25	4.32	15.37	15.31	15.43
57368.9	6	11.06	11.02	11.09	4.24	4.21	4.27	15.42	15.36	15.48
57371.4	6	11.03	10.99	11.06	4.25	4.22	4.29	15.38	15.32	15.44
57374.4	6	11.03	11.00	11.07	4.25	4.22	4.28	15.39	15.34	15.45
57377.2	6	11.01	10.97	11.04	4.25	4.22	4.28	15.38	15.32	15.44
57380.9	6	11.03	10.99	11.06	4.26	4.23	4.29	15.37	15.31	15.43
57383.2	6	10.97	10.94	11.00	4.22	4.19	4.25	15.41	15.35	15.47
57385.9	6	11.02	10.98	11.05	4.25	4.22	4.28	15.38	15.32	15.43

MJD	$N_{\text{obs}}$	$\log(L)$	$\log(L_-)$	$\log(L_+)$	$\log(T)$	$\log(T_-)$	$\log(T_+)$	$\log(R)$	$\log(R_-)$	$\log(R_+)$
57393.3	6	10.99	10.96	11.02	4.24	4.21	4.27	15.38	15.33	15.44
57396.7	6	10.93	10.89	10.96	4.22	4.19	4.25	15.39	15.33	15.45
57399.2	6	10.94	10.91	10.97	4.22	4.19	4.25	15.40	15.35	15.46
57427.7	6	10.80	10.77	10.83	4.21	4.18	4.24	15.35	15.29	15.40
57429.4	6	10.82	10.79	10.85	4.20	4.17	4.23	15.38	15.32	15.44
57433.1	6	10.75	10.72	10.79	4.16	4.14	4.19	15.42	15.37	15.48
57437.1	6	10.80	10.77	10.83	4.19	4.17	4.22	15.39	15.33	15.44
57447.2	6	10.77	10.73	10.80	4.19	4.16	4.22	15.37	15.32	15.43
57450.0	6	10.73	10.70	10.76	4.17	4.15	4.20	15.39	15.34	15.45
57453.9	6	10.79	10.76	10.82	4.21	4.18	4.24	15.35	15.29	15.40
57456.0	6	10.74	10.71	10.77	4.22	4.20	4.25	15.29	15.24	15.35
57457.5	5	10.69	10.66	10.72	4.16	4.13	4.19	15.39	15.34	15.45
57465.1	6	10.71	10.67	10.74	4.18	4.16	4.21	15.36	15.30	15.41
57470.2	6	10.74	10.71	10.77	4.20	4.17	4.23	15.34	15.28	15.39
57472.2	6	10.72	10.69	10.75	4.18	4.16	4.21	15.37	15.31	15.42
57475.6	6	10.72	10.68	10.75	4.21	4.18	4.23	15.32	15.26	15.37
57477.2	6	10.71	10.68	10.74	4.18	4.15	4.20	15.37	15.32	15.43
57480.0	6	10.64	10.61	10.67	4.17	4.15	4.20	15.34	15.29	15.40
57487.1	6	10.65	10.62	10.68	4.18	4.15	4.20	15.34	15.29	15.40
57489.0	6	10.63	10.60	10.66	4.18	4.16	4.21	15.32	15.26	15.37
57499.7	4	10.56	10.52	10.60	4.15	4.12	4.18	15.34	15.28	15.41
57502.7	6	10.63	10.60	10.66	4.19	4.17	4.22	15.30	15.25	15.36
57505.2	6	10.63	10.60	10.66	4.18	4.16	4.21	15.31	15.26	15.37
57508.9	6	10.65	10.62	10.68	4.19	4.16	4.22	15.32	15.26	15.37
57511.8	6	10.59	10.55	10.62	4.18	4.16	4.21	15.30	15.25	15.36
57516.1	6	10.61	10.58	10.64	4.19	4.16	4.21	15.30	15.24	15.36
57520.3	6	10.55	10.52	10.58	4.18	4.15	4.21	15.29	15.23	15.34
57523.7	6	10.57	10.54	10.60	4.19	4.17	4.22	15.27	15.21	15.32
57528.4	6	10.55	10.52	10.58	4.19	4.16	4.21	15.27	15.21	15.33
57533.6	6	10.51	10.48	10.55	4.13	4.11	4.15	15.37	15.31	15.42
57552.5	6	10.48	10.45	10.51	4.19	4.17	4.22	15.22	15.17	15.28
57554.8	6	10.62	10.59	10.66	4.10	4.08	4.12	15.48	15.43	15.53
57557.2	6	10.43	10.40	10.46	4.19	4.17	4.22	15.20	15.14	15.26
57560.0	6	10.47	10.44	10.50	4.23	4.21	4.26	15.14	15.08	15.19
57563.0	6	10.51	10.47	10.54	4.20	4.17	4.23	15.22	15.16	15.28
57569.1	6	10.61	10.57	10.64	4.09	4.07	4.11	15.50	15.44	15.55
57577.8	6	10.48	10.45	10.51	4.20	4.17	4.23	15.21	15.15	15.26
57591.7	6	10.35	10.32	10.38	4.13	4.11	4.15	15.29	15.23	15.34
57600.9	6	10.34	10.31	10.38	4.15	4.13	4.17	15.24	15.19	15.30
57608.5	6	10.32	10.29	10.36	4.20	4.18	4.23	15.13	15.07	15.18
57611.5	6	10.25	10.22	10.28	4.18	4.16	4.21	15.13	15.07	15.18
57615.4	6	10.32	10.29	10.35	4.23	4.21	4.26	15.06	15.00	15.12
57622.5	5	10.29	10.26	10.33	4.21	4.18	4.24	15.09	15.04	15.15
57626.7	5	10.19	10.15	10.22	4.17	4.14	4.19	15.13	15.07	15.19
57630.4	4	10.33	10.29	10.38	4.24	4.21	4.27	15.06	15.00	15.12
57632.8	4	10.32	10.27	10.37	4.26	4.23	4.30	15.00	14.94	15.06
57640.0	6	10.21	10.18	10.24	4.18	4.15	4.21	15.12	15.06	15.17
57645.5	6	10.18	10.15	10.21	4.19	4.16	4.21	15.09	15.03	15.14
57654.2	5	10.27	10.24	10.31	4.19	4.16	4.22	15.12	15.06	15.18
57667.3	3	10.21	10.16	10.25	4.19	4.16	4.22	15.09	15.04	15.15
57677.3	3	10.20	10.15	10.24	4.18	4.15	4.21	15.11	15.05	15.17
57680.2	4	10.27	10.23	10.31	4.21	4.18	4.24	15.09	15.03	15.15
57682.5	6	10.18	10.15	10.21	4.17	4.15	4.20	15.12	15.06	15.17
57687.0	3	10.21	10.17	10.26	4.22	4.19	4.25	15.04	14.98	15.09
57688.9	5	10.21	10.18	10.25	4.23	4.20	4.26	15.01	14.96	15.07
57704.0	2	10.27	10.19	10.36	4.05	4.01	4.08	15.41	15.31	15.51